

Chapter 4

Muon Arms Simulations

4.1 The Simulation Programs

4.1.1 Event Generators

Vector Meson Production

Vector meson resonances have been generated with code based on Vogt's parameterizations [41] of the production cross sections, rapidity and p_T distributions in heavy ion reactions.

Charm Production

Heavy flavor meson decays have been generated by two methods: Code based on Vogt's NLO calculations [42]; and HIJING [43] based on PYTHIA (for hard scattering) and FRITIOF (for soft scattering).

Drell-Yan Production

Drell-Yan production is given by a parameterization of results calculated from the CERN PDFLIB structure function library. The newest code allows one to chose the structure function set interactively. Absolute cross sections are put in by hand.

Backgrounds

The heavy ion event generator code HIJET [44] was used to generate minimum bias heavy ion events for pattern recognition and occupancy studies. HIJET is a p-nucleus and nucleus-nucleus event generator which allows projectile nucleons to successively traverse the target nucleus. When the distance of closest approach with a target nucleon is within the radius of $\sigma(\text{pp})$ 33 mb, an interaction is defined. ISAJET is then called. The produced particles are transformed back to the target frame. The forward leading baryon continues to traverse the target nucleus until it exits, and the back-leading baryon is returned to the target array. HIJET employs the MINBIAS routine of ISAJET. Secondary interaction is performed for

both the target and projectile in a symmetric fashion. Cascading of struck nucleons from the target and projectile are made. A Woods-Saxon, or spherical distribution of nucleons is used, with a hard core repulsion.

The UA1 event generator [45] is also used to calculate backgrounds. This consists of a pre-defined number of pions having a Gaussian rapidity distribution whose width, along with the transverse momentum spectra is scaled from the $p - p$ collision data obtained in the CERN UA1 experiment.

4.1.2 Detector Simulations

The PISA/PISORP [46] GEANT-based Monte Carlo simulation package was used to study the performance of the PHENIX muon system. In almost all simulations, the PISA package tracks particles produced by the above event generators through the PHENIX detector, creates secondaries, and stores the hit positions of all particles in all active detectors was used. When a simulation of the detector response was necessary, the output of the PISA code was used to run the PISORP code which includes simulation of the detector responses, and the track reconstruction codes.

4.2 Muon Tracking Performance Simulations

4.2.1 Detector Geometry

The baseline simulation CSC configuration of the muon tracker consists of three tracking stations located at z positions of 180.0, 348.5 and 600 cm for the North muon arm and z positions of 180.0, 288.5 and 450.0 cm for the South muon arm. Each station consists of three chambers which have a coarse cathode readout plane, an anode readout plane, and a fine cathode readout plane. The baseline CSC chamber has coarse cathode strips which are 1 cm wide, anode wires which are spaced 1 cm, and fine cathode strips which are 0.5 cm wide, but are read out on a 1 cm pitch with the strips capacitively coupled to each other. The anode-cathode plane spacing is 0.35 cm. The resolution of the fine cathode plane is expected to be 100 μm , so a noise level of 1% that produces approximately 100 μm resolution in the fine cathode plane is the baseline. The coarse cathode strips are 22.5° relative to the fine cathode strips and the anode wires are 90° relative to the fine cathode strips.

The passive material in front of the North muon arm consists of some or all of the following in our simulations: 1) a 28- cm thick copper nosecone in front of the central magnet yoke, 2) approximately 59- cm thick steel central magnet yoke, 3) 45 cm of borated polyethelene (neutron absorber), 4) 7 cm of lead shielding following the polyethelene and 5) a copper piston plug which sits next to the beamline, inside the polyethelene and lead shielding. As will be shown later, the polyethelene and lead absorber material have been removed in the baseline design because simulations have indicated that it provides little background reduction at the expense of degraded mass resolutions. The South muon arm material is the same as the North muon arm except that the nosecone is approximately 12 cm thick and begins at a larger z -value relative to the interaction point. A picture of the full muon geometry that is in the simulations is shown in Figure 4.1.

4.2.2 Detector Response

The CSC detector response model in PISORP is based on the theoretical work done by Mathieson [47] and experimental work which verifies Mathieson's work [48].

For the cathode strips, the Mathieson function [47] has been used to represent the amount of charge that would be deposited on strips of a given input geometry. The total amount of charge deposited in a chamber is selected from a Landau distribution. For the coarse cathode strips, the charge is deposited on the strips, a threshold cut is applied, and all strips with charge above the threshold cut are grouped into clusters. The measured position is taken as the average strip position of a given cluster.

For the fine cathode strips, the charge is distributed across strips of 0.5 cm pitch and the charge on every other strip (which are not read out) is divided by two and added to the neighboring readout strips to simulate the capacitively coupled strips. An input noise level, from a Gaussian distribution with a mean of 0.0 and an input σ value is then added to each strip. A threshold cut is then applied and all remaining strips with charge are grouped into clusters. These clusters are then fit to one or more Mathieson distributions depending on how many tracks the pattern recognition determines contribute to the cluster. The resulting

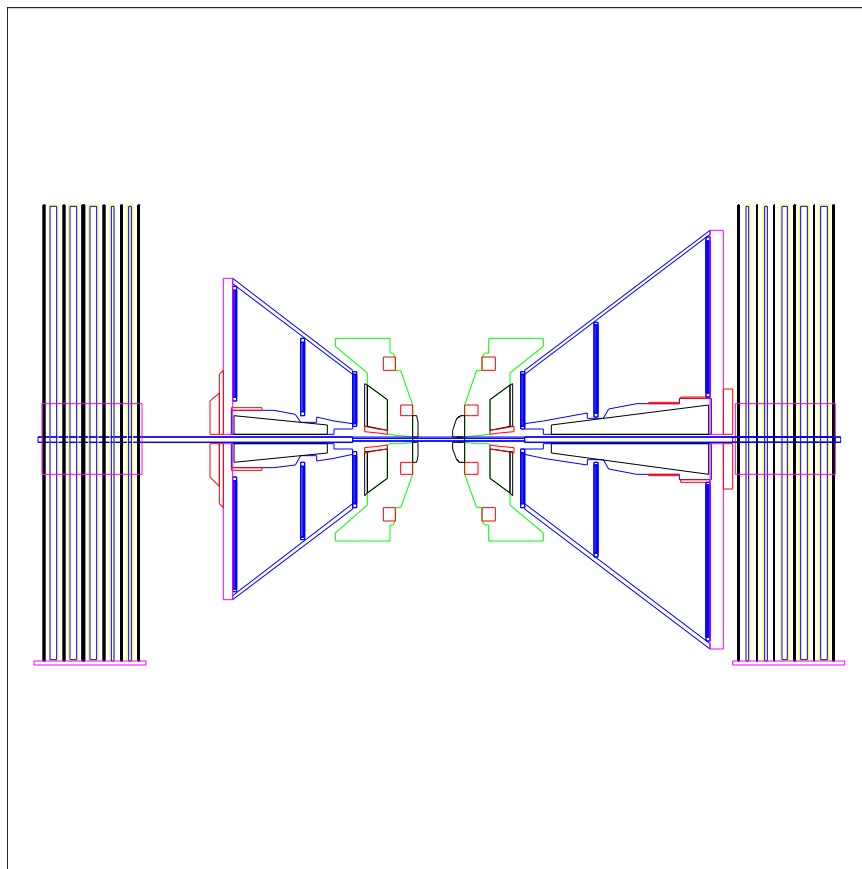


Figure 4.1: PISA geometry for the muon arms.

centroid is taken as the measured position of the track.

Anode responses are simulated by turning on the nearest wire to the true hit and applying a threshold cut.

4.2.3 Pattern Recognition and Track Reconstruction

Pattern recognition studies were performed using a stand-alone code which took the output muon tracking detector hits from PISA and reconstructed tracks using the Principle Component Analysis (PCA) method [49]. The full CSC response simulation was not available at the time of the pattern recognition studies, so the response was simulated by smearing the chamber hits by a given input resolution. The fine cathode hits were smeared using a Gaussian distribution and the anode and coarse cathode strips were smeared using a flat distribution that was as wide as the cathode strip or anode wire pitch. Hits that occurred within 3 cm of each other on the fine cathode strips were smeared by 4.5 times the nominal detector resolution to represent the resolution degradation that results from overlapping charge distributions. The track reconstruction that was used to determine the momentum and mass resolutions of the muon arms was based on the GEANE [50] package of GEANT, using the Kalman filter [51] fitting option. This package was put into PISORP and used the

full detector response simulations described above. In the track reconstruction the particle is iteratively swum through the tracking stations and the absorber material back to the vertex point (which is measured by the MVD) until the best least-squares fit to the measured points is achieved. The baseline MVD vertex resolution that was used was 1.0 mm in z and 400 μm in the $x - y$ plane which should represent the worst-case MVD vertex resolution (the resolution that the MVD quotes for low-multiplicity events).

4.2.4 Momentum and Mass Resolutions

Momentum Resolutions

Inclusive muon production at high- p_T ($p_T > 20 \text{ GeV}/c$) in pp collisions at $\sqrt{s}=500 \text{ GeV}$ is dominated by the weak boson production. The momentum of these muons ranges from $\sim 40 \text{ GeV}/c$ to $\sim 100 \text{ GeV}/c$ or more [20]. The momentum of the muons in the mid- p_T region ($5 \text{ GeV}/c$ to $10 \text{ GeV}/c$), which is dominated by the semi-leptonic decays of bottom quark, ranges from $10 \text{ GeV}/c$ to $30 \text{ GeV}/c$. The momentum of muons from Υ -decays ranges from $5 \text{ GeV}/c$ to $30 \text{ GeV}/c$. Hence, the performance of the muon tracking system should be studied over a wide energy range. Therefore, we have studied the momentum resolution of the muon system at momenta of 2, 3, 5, 7, 10, 30, and 100 GeV/c , with the baseline chamber resolution of 100 μm , and without the polyethelene or lead absorbers.

In our tracking system, the integrated magnetic field, $\int Bdl$, depends on the polar angle. The four points of polar angle, 15° , 20° , 25° , and 30° , have been chosen for this study, where the $\int Bdl$ values are as listed in Table 4.1¹.

	15 deg	20 deg	25 deg	30 deg
North Arm	7311.33	4921.06	3594.15	2775.69
South Arm	7737.99	4937.44	3442.67	2549.40

Table 4.1: The integrated magnetic field, $\int Bdl$, in Gauss \times m for each arm obtained by W. Sondheim.

Typical spectra for the fitted momenta (momenta predicted at the interaction point) for the North muon arm are shown in Figure 4.2. The momenta are divided by the input momenta. The long tail towards the low momentum side, which is significant in the lower input momenta, is due to the energy straggling in the material. The spectrum becomes symmetric for the higher input momentum, because the spatial resolution becomes the dominant source of the momentum resolution. All spectra have been fitted to a single Gaussian to extract the momentum resolution.

The obtained momentum resolutions are plotted in Figure 4.3 as functions of momentum for each polar angle for the North muon arm, the South muon arm, and the ratio of the two

¹Some geometric and coil modifications have been made to the magnet design (as outlined in the magnet section) since these simulations, but the $\int Bdl$ values have not changed significantly.

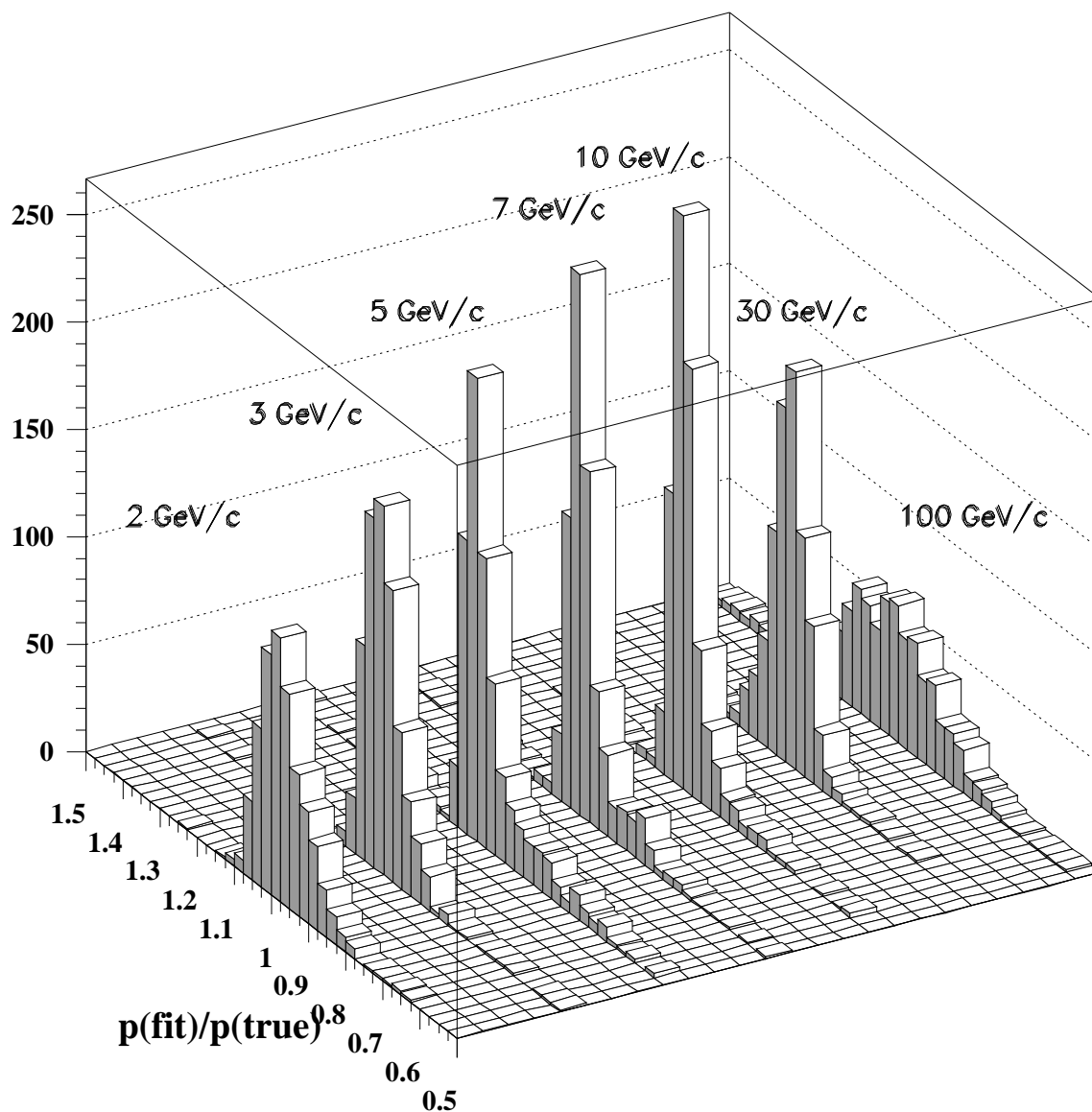


Figure 4.2: Momentum resolution spectra at 30° in the North muon arm. The momentum resolution is shown as a ratio of the fitted momentum to the input momentum. All spectra correspond to 1,000 single muon events.

arms. The lines show the results of the fit to the formula,

$$\frac{\sigma_p}{p} = \sqrt{\alpha + \beta p^2 + \frac{\gamma}{p^2}}. \quad (4.1)$$

Here α , β , and γ are the fitting parameters. This parameterization is made on the assumption that the momentum resolution originates from the multiple scattering, energy straggling and the measurement error on spatial positions. As can be seen, at low momenta where the resolution is dominated by straggling in the absorber material the South muon arm performs

slightly better than the North muon arm because of the smaller amount of absorber material present. At larger momenta, the North arm performance is better because of the longer lever arm through the magnetic field.

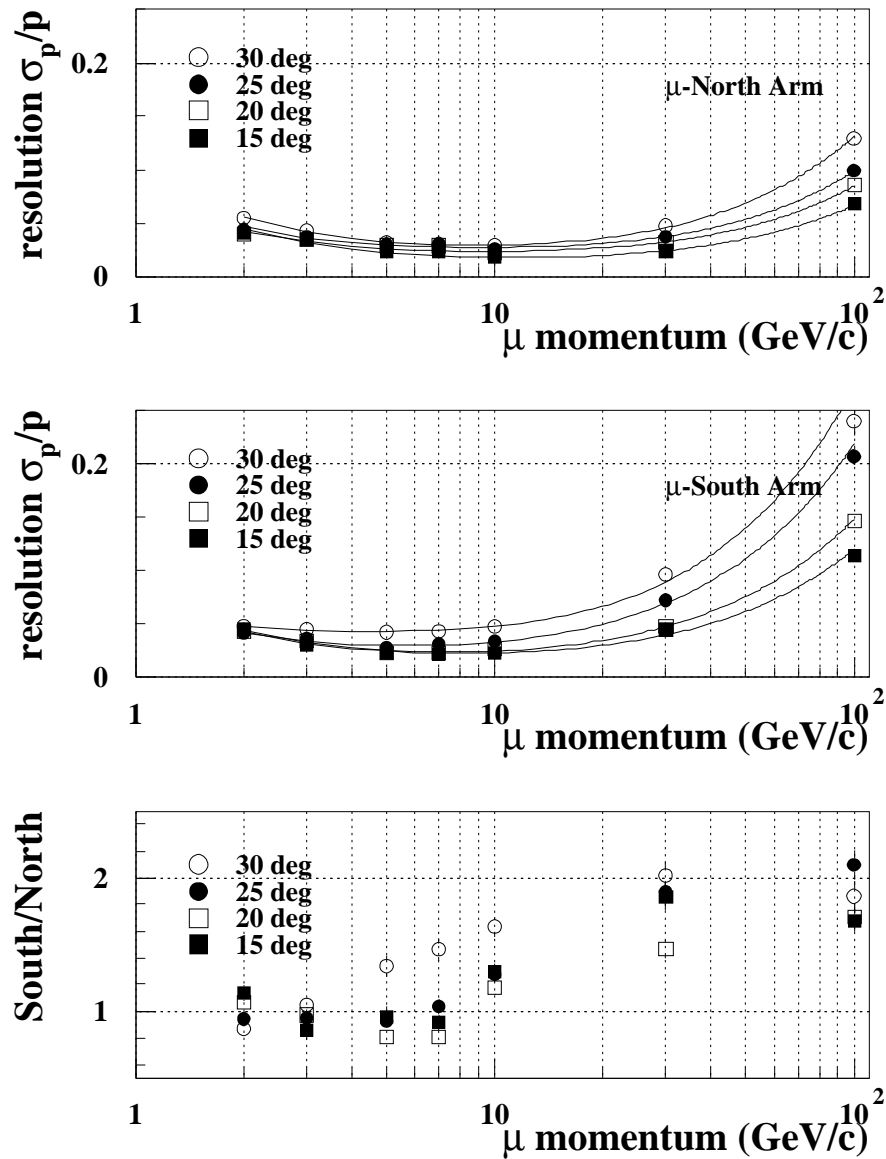


Figure 4.3: Momentum resolution as functions of input muon momentum at several polar angle points for the two muon arms.

Mass Resolutions

The mass resolution of the Υ is determined by both the energy straggling and multiple scattering in the absorber material as well as the chamber resolutions since the decay muons are of high enough momentum (on the order of 10 GeV/c on the average) that the chamber

resolution can contribute significantly to the sagitta measurement. The momenta of J/ψ and ϕ decay muons, on the other hand, are low enough that the mass resolution is completely dominated by the energy straggling and multiple scattering in the absorber material. We have therefore carefully studied the dependence of the Υ mass resolution on the tracking chamber resolutions, and the dependence of all of the mass resolutions on the absorber material in front of the tracking stations in order to optimize the design of the muon tracking stations and absorber materials.

Mass Resolution versus Chamber Resolution

The mass resolution of the Υ versus chamber resolutions was studied to determine what chamber resolution is necessary to obtain the mass resolution required to separate the Υ and Υ' states. Section 2.1 stated that the required mass resolution is approximately $200 \text{ MeV}/c^2$. Figure 4.4 shows the mass resolution versus chamber resolution for the North arm. As can be seen, a chamber resolution of approximately $100 \mu\text{m}$ produces a mass resolution of slightly more than $200 \text{ MeV}/c^2$. Since this resolution meets our physics criterion and has been achieved with a prototype chamber, our baseline chamber resolution will be $100 \mu\text{m}$. This corresponds to a chamber noise level of 1%. If better chamber resolution can be achieved, then the mass resolution can be improved slightly. However, the multiple scattering and energy straggling limit is $180 \text{ MeV}/c^2$. The South muon arm, however, has a significantly worse mass resolution versus chamber resolution because of the shorter length of the tracking arm (see Figure 4.5). The baseline chamber resolution of $100 \mu\text{m}$ produces a mass resolution of $260 \text{ MeV}/c^2$. In order to improve the mass resolution (to roughly the same performance as the North arm) in the baseline configuration where there are three chambers per station and only one fine cathode plane per chamber, the chamber resolution would have to improve to $50 \mu\text{m}$. However, since the momentum measurement error is more heavily weighted by the error in the middle station measurement, if just the station 2 resolution were improved, the mass resolution would improve significantly. This is illustrated in Figure 4.6 where the Υ mass resolution is shown versus station 2 chamber resolution. Alternatively, if station 2 were changed from 1 fine cathode plane per chamber to 2 fine cathode planes per chamber, the station resolution would improve by $\sqrt{2}$ and the mass resolution would improve to approximately $220 \text{ MeV}/c^2$.

The mass resolutions of ϕ and J/ψ vector mesons for the North and South muon arms are shown in Figure 4.7 for the baseline absorber configuration, which does not include the polyethelene or lead absorber. At these low masses, the resolution is dominated by the energy straggling in the absorber material in front of the tracking stations, so the South arm performs slightly better than the North muon arm because of the smaller amount of absorber material in the copper nosecone.

With the two muon arms, it is also possible to study the Υ production that produces one muon in each arm. The mass resolution for these events is affected by the fact that the muon momentum is significantly smaller than when the decay muons both enter one arm. Although the momentum resolution inside the tracking regions is better at the smaller momenta, the energy straggling and multiple scattering in the absorber materials contribute more significantly to the mass resolution. The mass resolution for Υ muons entering the

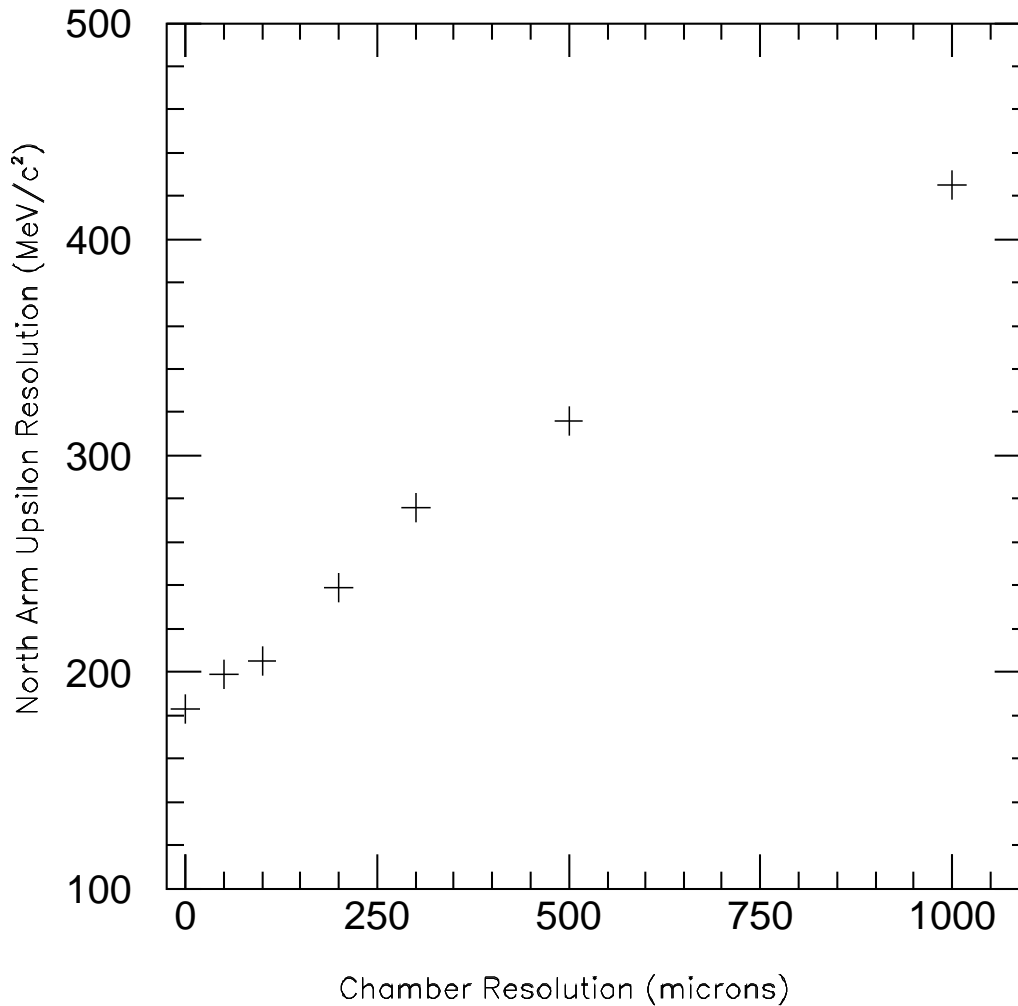


Figure 4.4: Υ mass resolution versus chamber resolution in the North muon arm.

two arms is shown in Figure 4.8. The central mass region is similar to the North muon arm performance, but the long energy straggling tail produces a gaussian fit resolution of $250 \text{ MeV}/c^2$. The only way to significantly improve this resolution would be to reduce the amount of absorber material present in front of the tracking stations.

Nosecone and Absorber Studies

The baseline muon arms have asymmetric nosecones with the North arm having a copper nosecone which begins at $z=32 \text{ cm}$ and extends to $z=60 \text{ cm}$, while the South arm has a nosecone which begins at $z=-48 \text{ cm}$ and extends to $z=-60 \text{ cm}$. The nosecone in the North arm was originally chosen to extend to smaller z values to improve the signal to noise ratio

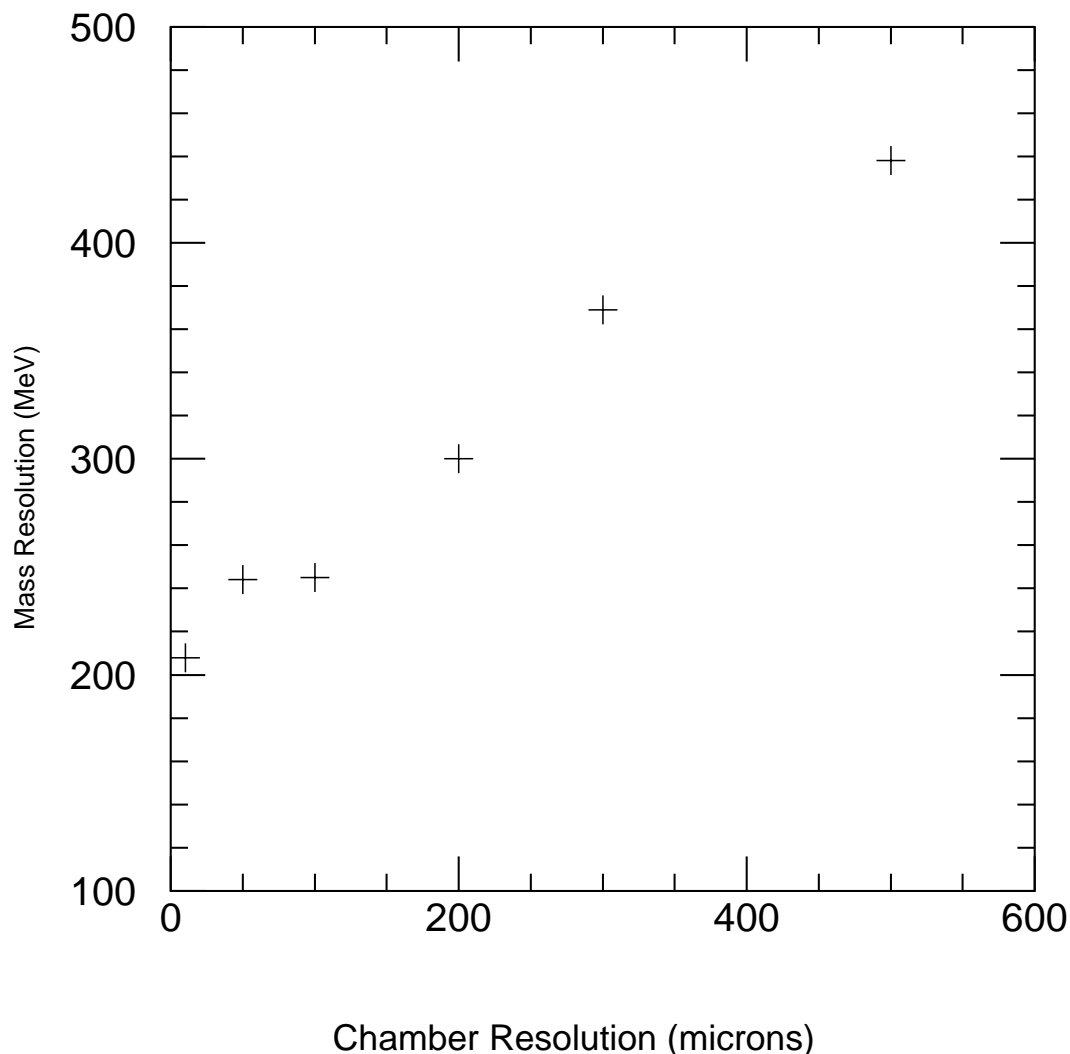


Figure 4.5: Υ mass resolution versus chamber resolution in the South muon arm.

at the ϕ and J/ψ masses [1] by reducing the number of pions and kaons that are able to decay to muons before reaching the tracking stations. A systematic study of the advantages and disadvantages of having asymmetric nosecones or symmetric nosecones needs to be completed.

The polyethelene and lead absorber materials were originally introduced into the muon tracking design to reduce the number of background neutrons, photons and electrons entering the muon tracking chambers. Since the addition of absorber material degrades the mass resolution of the lower mass vector mesons, a systematic study of the trade-off of background rates in the muon tracking chambers versus mass resolution degradation was performed. A copper plug which surrounds the beam pipe and lies between the central magnet yoke and

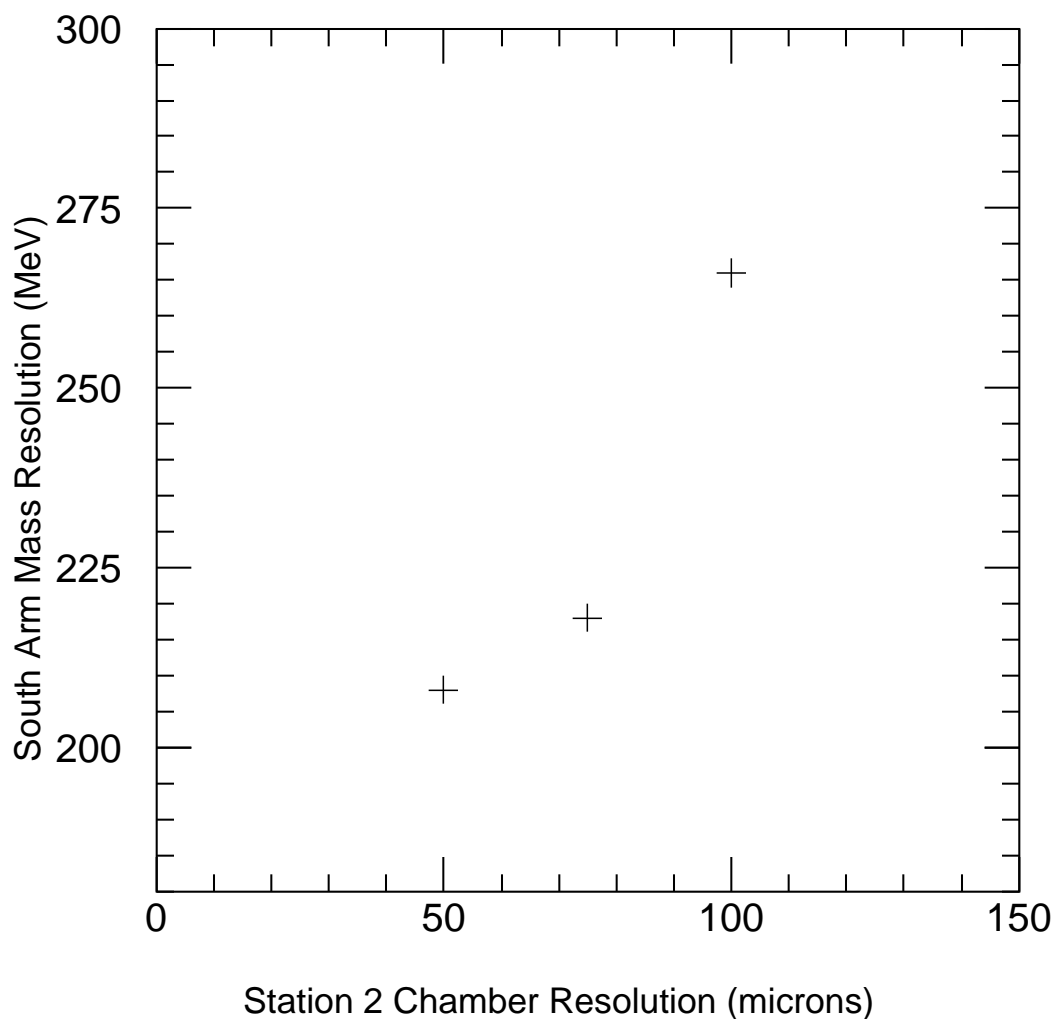


Figure 4.6: Υ mass resolution versus station 2 chamber resolution in the South muon arm. Stations 1 and 3 have 100 μm chamber resolution.

the station 1 tracking chambers significantly reduces the rate of particles in the tracking stations, but since it is outside of the acceptance of the tracking stations it does not affect the mass resolutions. Therefore, it will remain in the baseline.

Figures 4.9 and 4.10 show the mass resolutions of the ϕ , J/ψ and Υ vector mesons with and without the polyethelene and lead absorbers present. As can be seen, the degradation of the ϕ and J/ψ resolutions is significant in both muon arms.

On the other hand, Table 10.2 in the CDR Update [2] shows the background rates of charged and neutral particles in the tracking stations with and without the absorber material present. It is expected that the neutron efficiency of the chambers will be small enough that

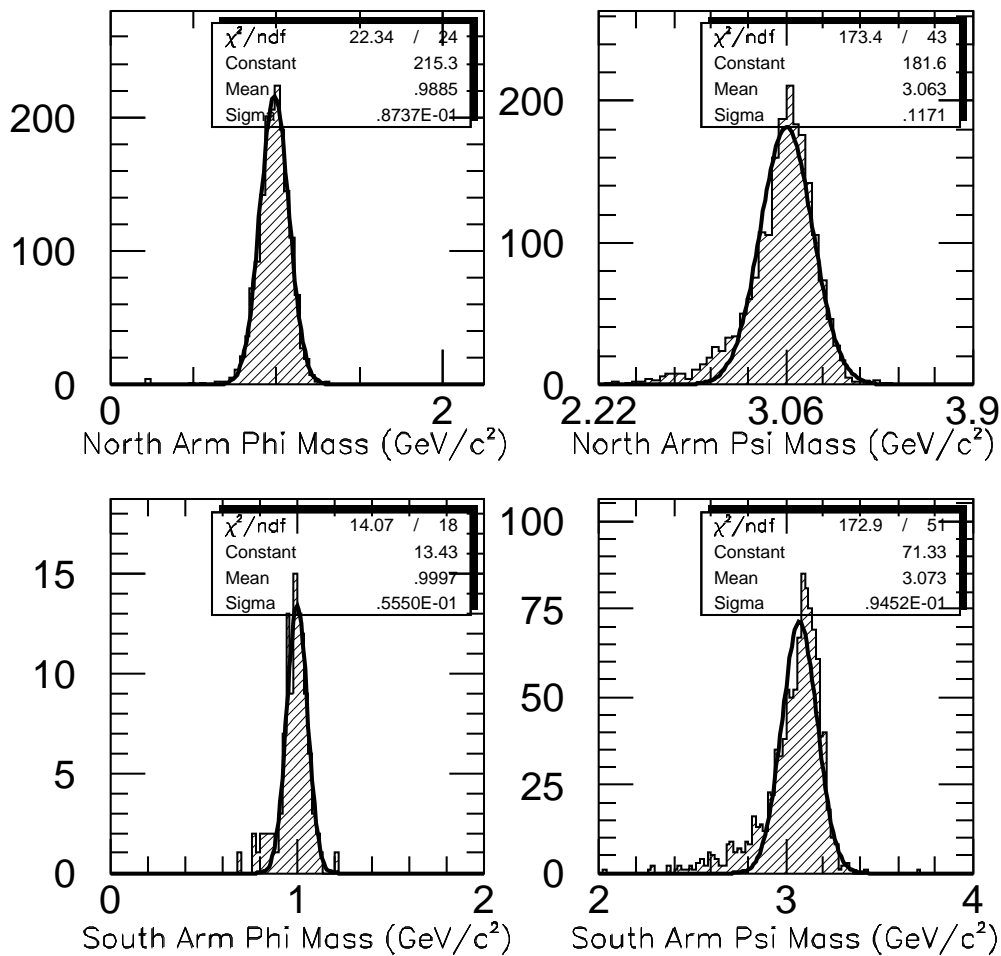


Figure 4.7: ϕ and J/ψ mass resolutions for the baseline North and South muon arms.

a significant reduction of the neutrons exiting the central magnet steel will not be necessary. The charged particle rate is only reduced by a factor of 1.3 and the peak occupancies, near the muon magnet piston, are not reduced much at all as long as the copper piston plug is always in place (see Figures 4.11 and 4.12 where the relative radial distributions of charged particles are shown with and without the absorber materials present). We have therefore chosen to remove the polyethelene and lead absorber material from the baseline design. More detailed studies may show that a small amount of absorber material is advantageous, but not the 50+ cm that was put into the previous baseline design.

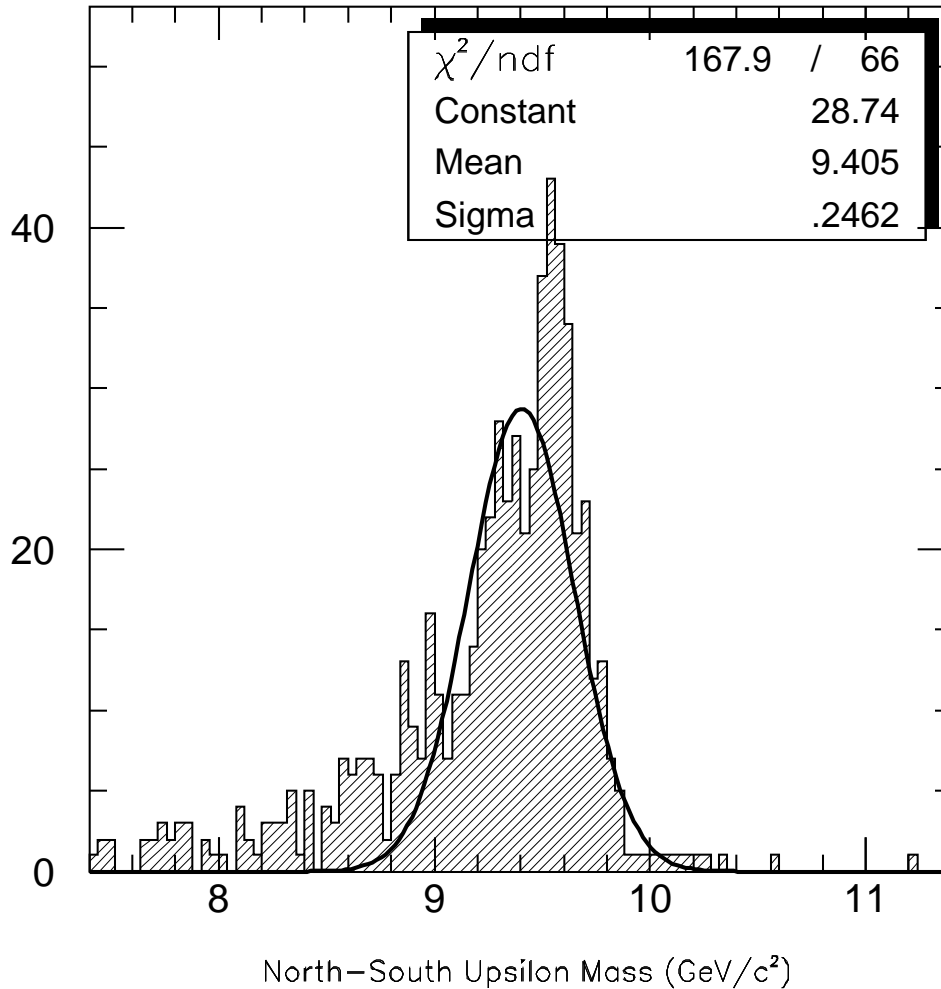


Figure 4.8: Υ mass resolution for Υ decays which produce one muon in each muon arm.

Chamber Occupancies

The relative occupancy of the station 1 chambers versus radial distance was shown in Figures 4.11 and 4.12 and the absolute occupancy of the 9 CSC chambers in the North arm in HIJET events is shown in Figure 4.13. As can be seen, the occupancies are relatively small away from the muon magnet piston area ($r=0.32$ m) but increase rapidly near the piston. Because of this, track finding at large θ angles in the muon arm can be expected to be rather straightforward because of the low occupancies, but for ϕ and J/ψ vector mesons, which tend to populate the chambers at small θ , the track finding will be more difficult. However, the CSCs provide the capability of both resolving ghost points within a single chamber because of the stereo angles of the anode wires, coarse cathode strips, and fine cathode strips, and of

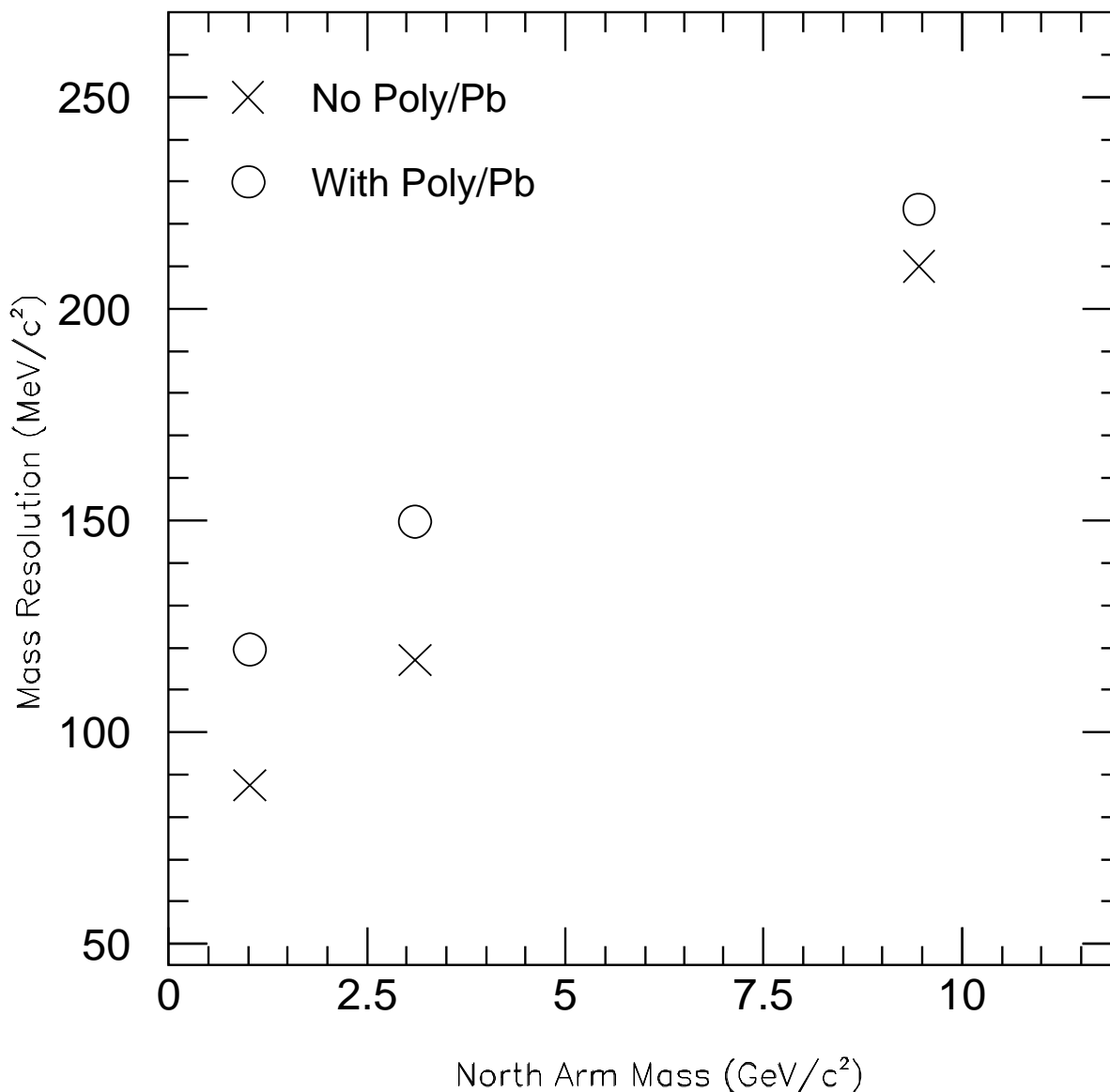


Figure 4.9: Vector mass resolutions with and without the polyethelene and lead absorbers present in the North muon arm.

resolving overlapping hits to a high degree by fitting the charge distribution with multiple peaks [52]. Because of this, the technology choice of CSCs over drift chambers for the tracking chambers should improve our capabilities of track finding at small θ .

The occupancies in the South muon arm are somewhat better at small angles because of the larger piston angle (10° in the North muon arm and 12° in the South muon arm) and somewhat larger at large angles because of the smaller amount of absorber material in the nosecone. (See Figure 4.12).

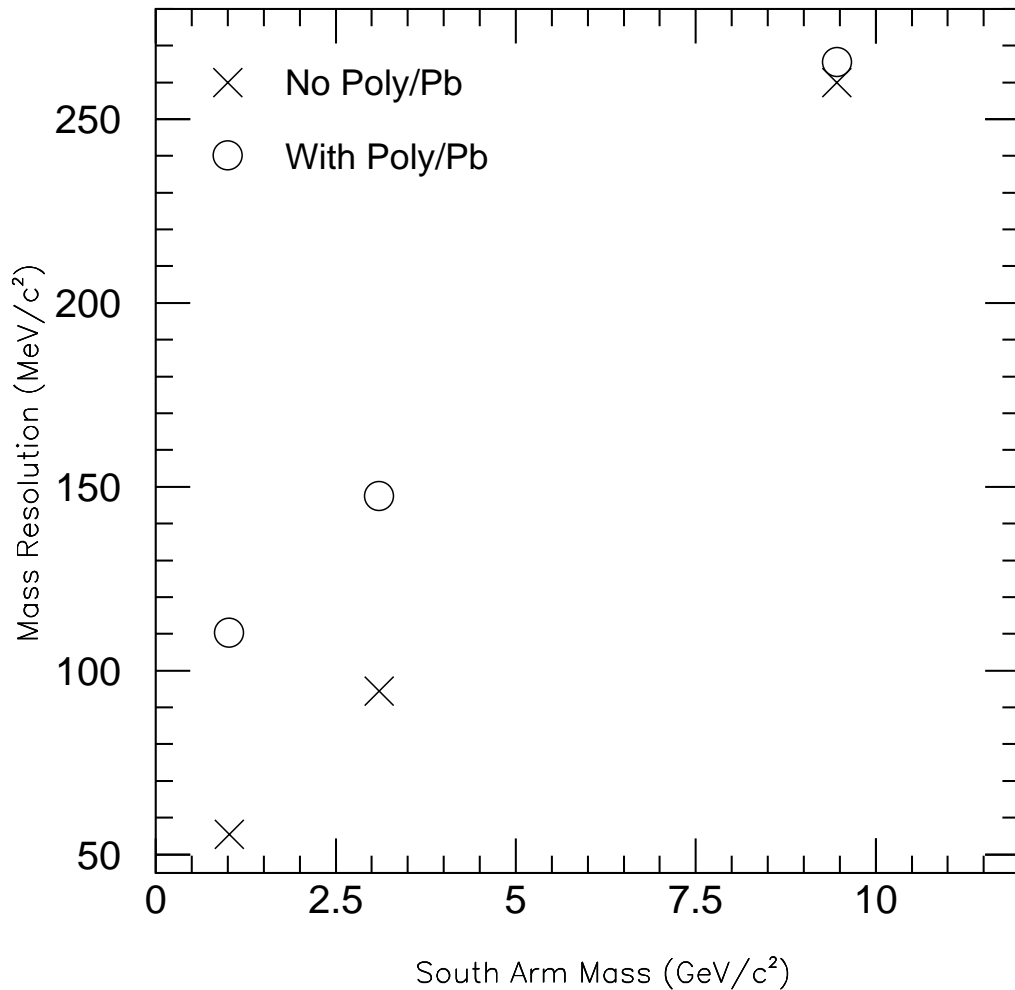


Figure 4.10: Vector mass resolutions with and without the polyethelene and lead absorbers present in the South muon arm.

4.2.5 Muon Tracking Performance

The track finding efficiency for the baseline CSCs in the North muon arm was calculated for muon tracks from Υ s embedded in a single HIJET background per reconstructed event for chamber resolutions of 100, 200, and 300 μm . One hundred of these events were run for each resolution, and the results are shown in Table 4.2. As can be seen, there was no noticeable change in efficiency under the three conditions. Because of this, the track finding efficiency capabilities of the tracking system place no further constraints on the resolution required by our chambers.

The track finding efficiency versus occupancy was determined by performing track finding

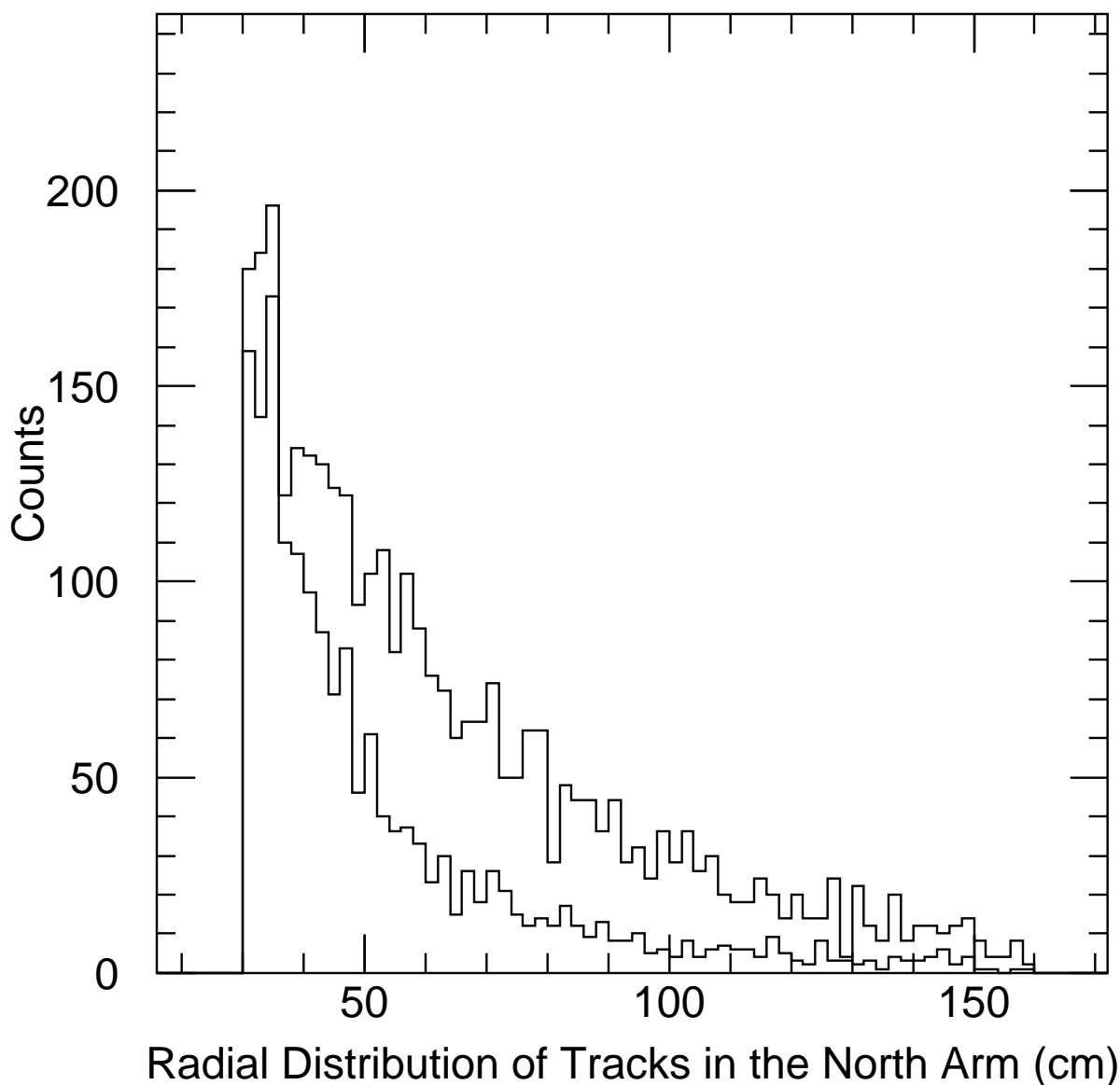


Figure 4.11: The relative radial distribution of HIJET event charged particles in the North muon arm, station 1, with and without the polyethelene and lead absorbers. These distributions were produced by running many hijet events through the PISA detector, with and without the polyethelene present.

on Υ events with both one and two HIJET events of background per reconstructed event. The track finding with two HIJET events as background helped improve the statistics at higher occupancy. One hundred events of each type were run. The occupancy for a given chamber was calculated by counting the number of strips that were made active by the digitization portion of the code and dividing by the total number of strips in that particular chamber. The average occupancy of the three stations that a track passed through was used in the following tables which show efficiency versus occupancy. The efficiency was

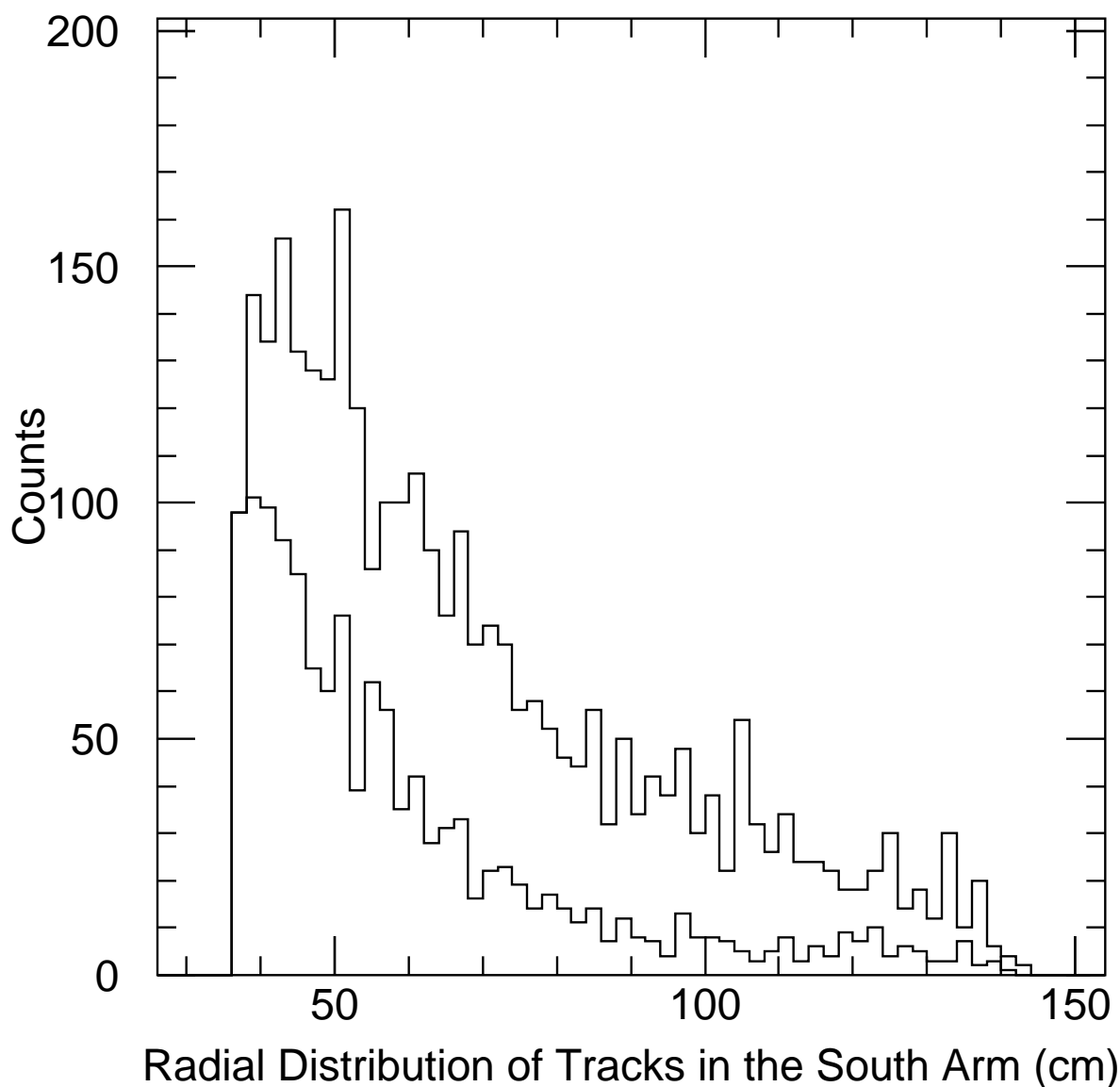


Figure 4.12: The relative radial distribution of HIJET event charged particles in the South muon arm, station 1, with and without the polyethelene and lead absorbers. These distributions were produced by running many hijet events through the PISA detector, with and without the polyethelene present.

determined by dividing the number of “good tracks” (tracks which passed through all three tracking stations) by the number of found tracks. The results of these runs are shown in Table 4.3 where the track finding efficiency is shown versus the average occupancy in the chamber that the track passed through and in Table 4.4 where the track finding efficiency is shown versus the average track multiplicity in the chambers that the track passed through.

The track finding efficiency was also calculated for a CSC configuration comprised of two chambers per station rather than three to indicate how the system would perform with

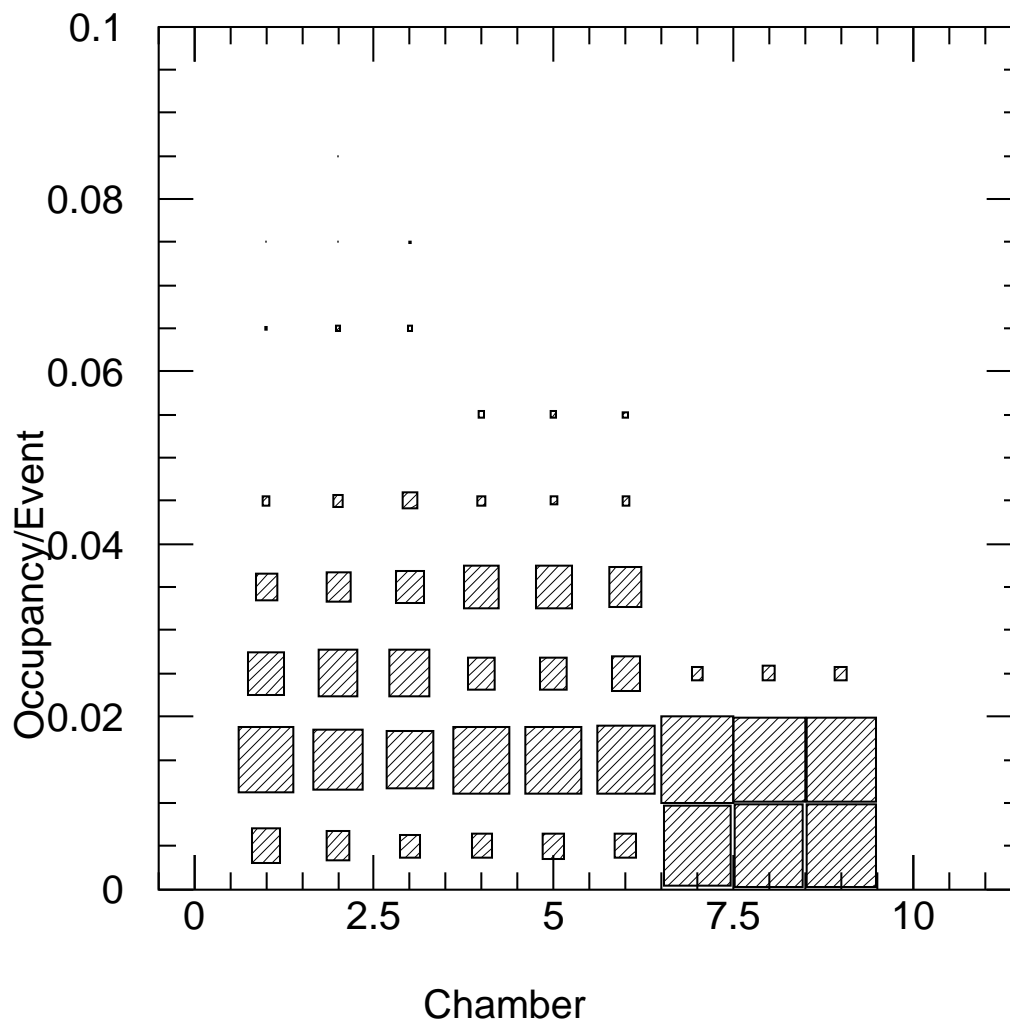


Figure 4.13: The absolute occupancy of the North arm chambers in HIJET events.

missing hits. The resulting track finding efficiency for $100 \mu\text{m}$ chamber resolution was 92% for 100 Υ events overlaid with single HIJET events. Therefore, we expect that the tracking system will perform well with missing hits, but we would still like to have three chambers per station for redundancy and to improve the momentum resolutions.

Chamber Resolution (μm)	Track Finding Efficiency
100	95 ± 2 %
200	96 ± 2 %
300	95 ± 2 %

Table 4.2: The track finding efficiency in the North muon arm for chamber resolutions of 100, 200, and 300 μm .

Occupancy in Chambers (%)	Track Finding Efficiency (%)
0-3	100 ± 1
3-5	96 ± 2
5-7	97 ± 2
7-9	92 ± 4
9-12	85 ± 6

Table 4.3: The track finding efficiency in the North muon arm different chamber occupancies.

Track Multiplicity in Octant	Track Finding Efficiency (%)
0-5	100 ± 5
5-10	97 ± 2
10-15	95 ± 2
15-20	96 ± 3
20-25	87 ± 6

Table 4.4: The track finding efficiency in the North muon arm different track multiplicities in the chambers.

4.3 Muon Identifier Performance Simulations

4.3.1 Triggering Performance

The mean occupancy in the muon identifier in gap 3 is only 1 hit per event for UA1 events (simulated central collisions without primary muons). Beam gas would be a more serious background (see below); however, we anticipate suppressing this background with shielding. We have developed a trigger algorithm which is very efficient for dimuons, yet has good background rejection. See Ref. [53] and [54] for a more detailed discussion of the trigger algorithm.

An acceptable dimuon Local Level 1 (LVL-1) trigger for Au-Au running requires the presence of both two or more roads as seen in the x -view and two or more roads as seen in the y -view. A valid view requires all three of the first three planes to have a hit. Each view points to the origin. In plane 1 it consists of a pair of staggered tubes. In planes 2 and 3, the view is 5 tubes wide (ie, ± 2 tubes). There are a total of 749 possible trigger views. For beam gas rejection, we further reject views which are completely parallel to the beam line (and more than 100 cm from the beam line to maintain signal efficiency). We do not choose to phrase the LVL-1 algorithm in terms of $x - y$ intersections in order to minimize the number of possible LVL-1 trigger roads. (There are on the order of 10^4 $x - y$ intersections in a muon identifier plane.) Different running conditions (such as pp collisions for spin physics) will have different backgrounds and will employ somewhat different trigger requirements using the same electronics.

Simulations have shown that the estimated occupancies are low enough in the muon identifier that the ambiguities associated with hodoscopic readout of a panel will not lead to an intolerable LVL-1 trigger rate. Moreover, such ambiguous $x - y$ intersections are immediately resolved upon matching with tracks in the muon tracker at LVL-2 and offline. These studies were used to justify using hodoscopic readout rather than external pads in order to avoid the costs associated with pad design, development, and fabrication. (The detectors are also thinner without pads and their associated connectors.)

Triggering Efficiency for Vector Mesons and Drell-Yan

For approximately 80% of J/ψ mesons, both muons penetrate to at least plane 3. Of these, 97.4% will satisfy the LVL-1 trigger algorithm described above. This rises to near 100% if the straight-view (beam-gas) rejection criterion is removed from the trigger algorithm.

Approximately 18% of ϕ mesons (satisfying generator requirements that both muons exceed 1.5 GeV/c and have a θ angle of between 10° and 35°) have muons which both penetrate to plane 3 of the muon identifier. Of those, 80% will satisfy the trigger requirements. The LVL-1 trigger efficiency is flat as a function of rapidity over almost the entire acceptance.

Impact of Beam-Gas

If not handled properly, beam gas is a potentially very serious background for the muon identifier LVL-1 trigger due to the large number of particles which can enter the detector [55].

We expect that specialized absorber shields located in the RHIC tunnel will be required to suppress this background. (See Ref. [56] and [57] for more details on how we have attempted to estimate this background including development of a new simulated beam gas event generator.) We have estimated that the raw beam-gas event rate is 16 kHz, which is to be compared to the 2 kHz rate of central Au-Au collisions. The design of the LVL-1 trigger plus shielding in the RHIC beam tunnel will be needed in order to keep this background trigger rate under control.

Note that this beam gas event background is mainly a concern for avoiding deadtime associated with the LVL-1 trigger. The background is strongly suppressed at LVL-2 and offline by matching to tracks in the muon tracker and requiring that the track come from within 40 cm of the interaction vertex. This is because tracks in beam gas events are typically parallel to the beam pipe.

4.3.2 μ/π Rejection Ratios versus Muon Momentum

Approximately 20% of UA1 events satisfy the LVL-1 trigger algorithm. Thus, the false LVL-1 trigger rate due to central collisions (and neglecting beam gas) is 20% of 2 kHz. This is an acceptable contribution to the total LVL-1 bandwidth and will not introduce dead time. Moreover, this background will be almost completely suppressed by LVL-2. We estimate that the occupancies in the identifier will be entirely tractable providing that the beam gas background is properly shielded.

In order to study the offline performance of the muon identifier, we use a parametrized Monte Carlo simulation of the tracking chamber performance [21]. We then match muon identifier roads to the smeared generated tracks in the tracker. Simulations indicate that the matching efficiency is 97%. We then subsequently require that the measured momentum be consistent with the depth penetration in the muon identifier for a muon. Our simulations impose a requirement which is 95% efficient for real muons.

Ultimately, the performance of the muon identifier should be capable of providing an overall μ/π separation ratio of approximately 10^{-4} in order to insure that the dominant backgrounds arise from pion and kaon decay in flight (instead of detector performance). That performance can be obtained after the LVL-2 trigger (or offline) by means of imposing four requirements: (1) the muon identifier road must match to a track in the tracker, (2) the track in the tracker must extrapolate to within 40 cm of the vertex in the transverse plane, (3) the muon road must have a correct depth-momentum relation, and (4) the invariant mass of the reconstructed dimuon must exceed 1 GeV/ c^2 . We have also studied using multivariate discriminant analysis techniques [58] [59] in order to investigate possible further improvements in μ/π separation offline.

4.4 System Performance Parameters

4.4.1 Alignment and Survey Requirements

The internal alignment requirements for the muon tracking system are rather stringent since a momentum resolution inside the tracking volume of less than 2% is required to obtain a good mass resolution of the Υ vector meson (2% momentum resolution corresponds to an Υ mass resolution of approximately 200 MeV/c²). In addition to the internal alignment requirements, the mass resolution requirements dictate alignment requirements of the muon tracking system relative to the MVD (or interaction point), the magnetic field, and the distance between the two muon tracking arms. In addition, there may be some requirement for alignment of the tracking stations relative to the central arm if muon identification systems are added to the central arm.

Internal Alignment Requirements

The internal alignment of the muon tracking stations in ϕ is determined by the momentum resolution requirements of the tracker. In order to obtain a mass resolution (which is dominated by energy straggling in the material prior to the tracking stations) on the order of 200 MeV/c² for the Υ vector meson, a spectrometer momentum resolution of less than 2% is required. Section 4.2.4 showed that this can be obtained by three tracking chambers at each measurement station which have a ϕ resolution of approximately 100 μm . In order to retain this momentum resolution, an alignment resolution of much less than 100 μm is desired. We specify a ϕ alignment criterion of 25 μm inside the tracking volume.

If muons which pass from octant 1 in station 1 to octant 2 in station 2, for example, are to be tracked then the octant-to-octant alignment requirements will be the same as the requirements specified above, determined by the momentum resolution requirements. If only tracks which pass through projective octants are to be tracked, then the octant-to-octant alignment requirements will be determined by the opening angle resolution needed to achieve good mass resolutions. The angular resolutions at the vertex are given in the section on aligning the North and South muon arms, and are on the order of 3-9 mRad. If that resolution, which is caused by the multiple scattering in the absorber materials, is to be maintained, then an octant-to-octant alignment on the order of 1.2 mm in the $x - y$ plane is adequate (see North and South arm alignment section).

The muon tracking station-to-station alignment in z affects the ability to measure the sagitta of a track (and thus the momentum) in the tracker, the alignment of the stations with the magnetic field, and the ability to measure the θ angle of a track (and thus the opening angle of dimuons from vector meson decay). To determine exactly what the z alignment requirements are, a GEANT study was done which took hits from Υ dimuons and displaced all station two hits by a fixed amount with respect to stations one and three. The hits at stations one and three and the displaced station two hits were then fit and the mass resolution of the dimuons was calculated. Figure 4.14 shows the resulting mass resolution vs. station two displacements. As can be seen 0.5 and 1.0 mm displacements did not affect the mass resolution, but a 1.5 mm displacement increased the mass resolution by 15% to

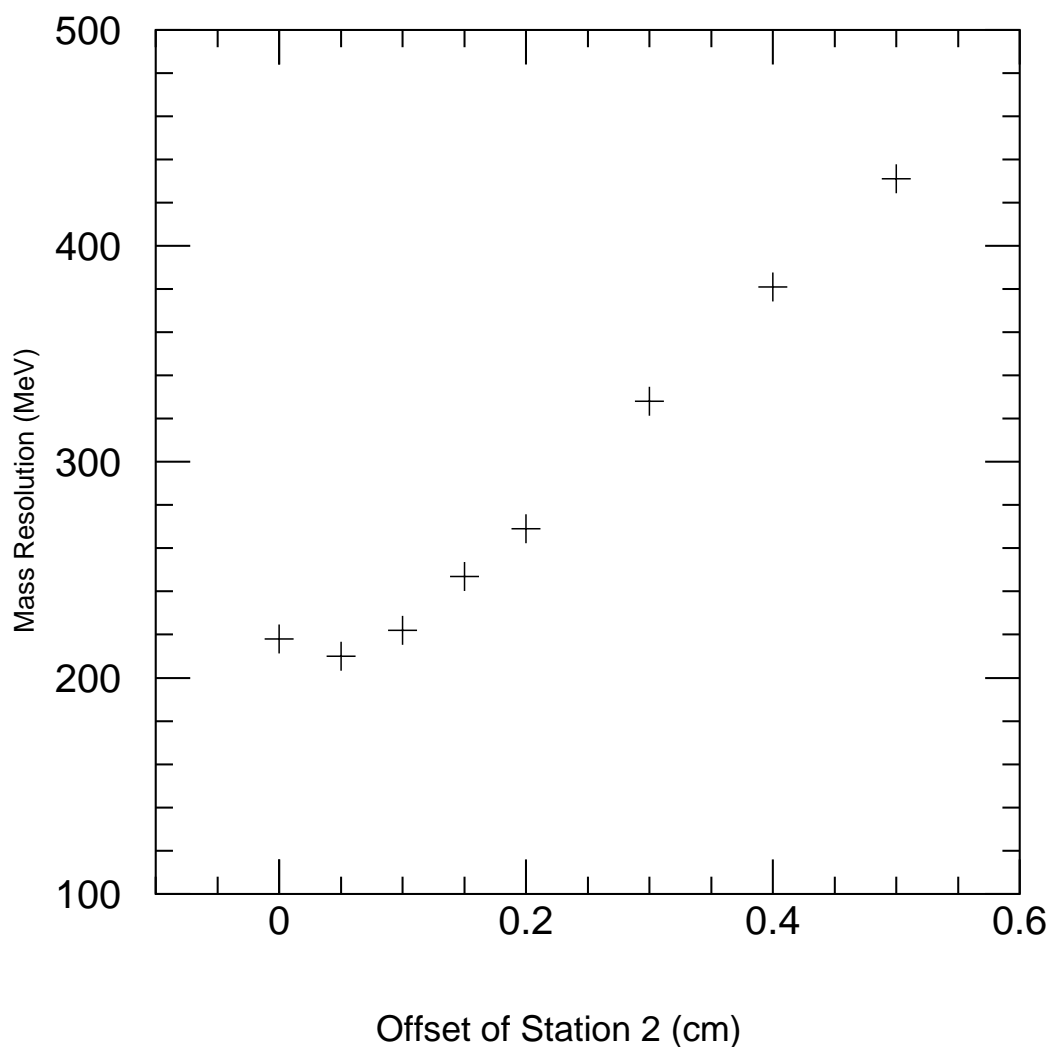


Figure 4.14: The Υ mass resolution in the North muon arm versus a displacement of the station two hits.

250 MeV/c^2 , and a 5 mm displacement increases the mass resolution to 430 MeV/c^2 . We therefore require a station to station alignment in z of at least $1.5/4 \text{ mm} = 0.4 \text{ mm}$.

Global Alignment Requirements

The spectrometer as a whole must be aligned to the muon magnet in order to accurately track through the very non-uniform magnetic field. It must be aligned relative to the measured vertex point in order to project the measured momentum vector in the spectrometer to the interaction point, and the North and South muon arms must be aligned relative to each other if dimuons which go into the two arms are to be measured. In addition, if muon identification

is added to the central arm then the muon arms will need to be aligned relative to the central tracking chambers.

Alignment to Magnetic Field Since the magnetic field in the muon tracking region is non-uniform, the tracking stations must be aligned to the field in order to accurately determine the momentum of tracks from their trajectory through the field. To determine what the exact alignment requirements are, the GEANT simulation code was used again. Muons from Υ decay were tracked through the magnetic field and their hits in the tracking stations were recorded. The hits were then fit to a trajectory using the same magnetic field map that produced the hits, but displacing it by a fixed amount in (x, y) , and z . The resulting mass resolutions versus the amount of displacement in the z direction are shown in Figure 4.15. For the (x, y) displacement, the input map was shifted from (x, y) to $(x+\text{offset}, y+\text{offset})$. The resolution versus ‘offset’ is shown in Figure 4.16.

As can be seen, the spectrometer as a whole can actually be displaced a fair amount before the mass resolution begins to suffer. The z displacement is the least sensitive since the magnetic field integral does not change quickly if the map is just displaced in the z direction. The magnetic field integral does change rather quickly with θ as shown in Table 4.1 so the mass resolution depends more strongly on a displacement in the x and y directions. No change in the mass resolution was seen for displacements up to 1 cm. A small increase in the resolution was seen for a displacement of 2.5 cm, and at 5 cm displacement the mass resolution increased by 20% to 256 MeV/c². Given these studies, we require that the spectrometer as a whole be aligned to the magnetic field to at least $2.5/4=0.6$ cm in x and y , and only has to be aligned to within several centimeters in the z direction.

Alignment to the Interaction Point The creation point of the vector mesons must be known so that the muon momentum vectors that are measured in the tracking stations can be projected through all of the absorber material to the vertex, and the original vector meson mass reconstructed. The GEANT reconstruction code uses an input resolution in z , and assumes the τ/ϕ interaction point is (0,0). To determine how the vertex resolution affects the projection of the momentum vector to the vertex, a perfect momentum resolution was taken inside the spectrometer, and the z resolution of the vertex was varied from perfect resolution to 2 cm resolution. The resulting mass resolutions (for the North muon arm) are shown in Figure 4.17. The mass resolution dependence on the z resolution was essentially the same when it was run for the South muon arm. As can be seen, the mass resolution does not begin to degrade until the resolution gets as large as 2 cm, and then it only degrades by approximately 7%. We therefore require that the spectrometer be aligned to the vertex to less than $2.0/4=0.5$ cm. The same requirement is applied to the $x - y$ plane giving an alignment requirement of 1-3.5 mm over the 10° - 35° acceptance of the spectrometer.

To see if displacement of the spectrometer with respect to the vertex provided a tighter alignment constraint than smearing the vertex resolution, the muon tracking stations as well as the magnetic field were displaced by a fixed amount relative to the interaction point, and vector mesons were reconstructed. The spectrometer could be displaced by 5.0 cm without a noticeable affect on the momentum resolution reconstructed at the vertex, which is larger

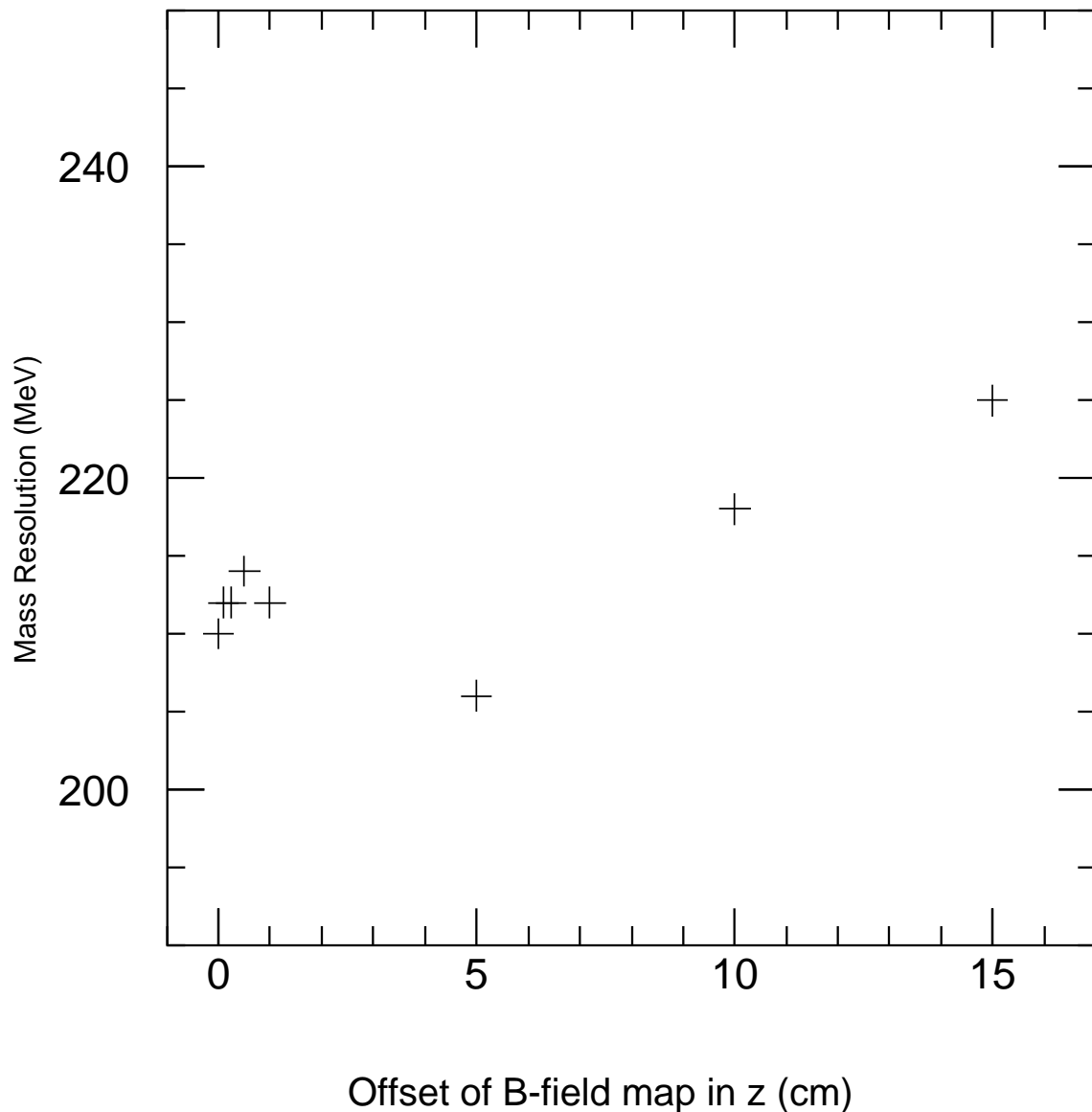


Figure 4.15: The Υ mass resolution in the North arm versus a z displacement of the magnetic field map.

than the other vertex constraint, so the alignment criterion stated in the previous paragraph will be used for the vertex alignment.

Alignment Between the North and South Muon Arms The North and South muon arms must be aligned relative to each other if vector mesons which produce one muon which goes into the North arm and one muon which goes into the South arm are to be reconstructed. The alignment requirement is determined by the opening angle resolution that is required to get a good mass resolution of these particles. Alternatively, we can make sure that the error in the angular measurement due to misalignments is much less than

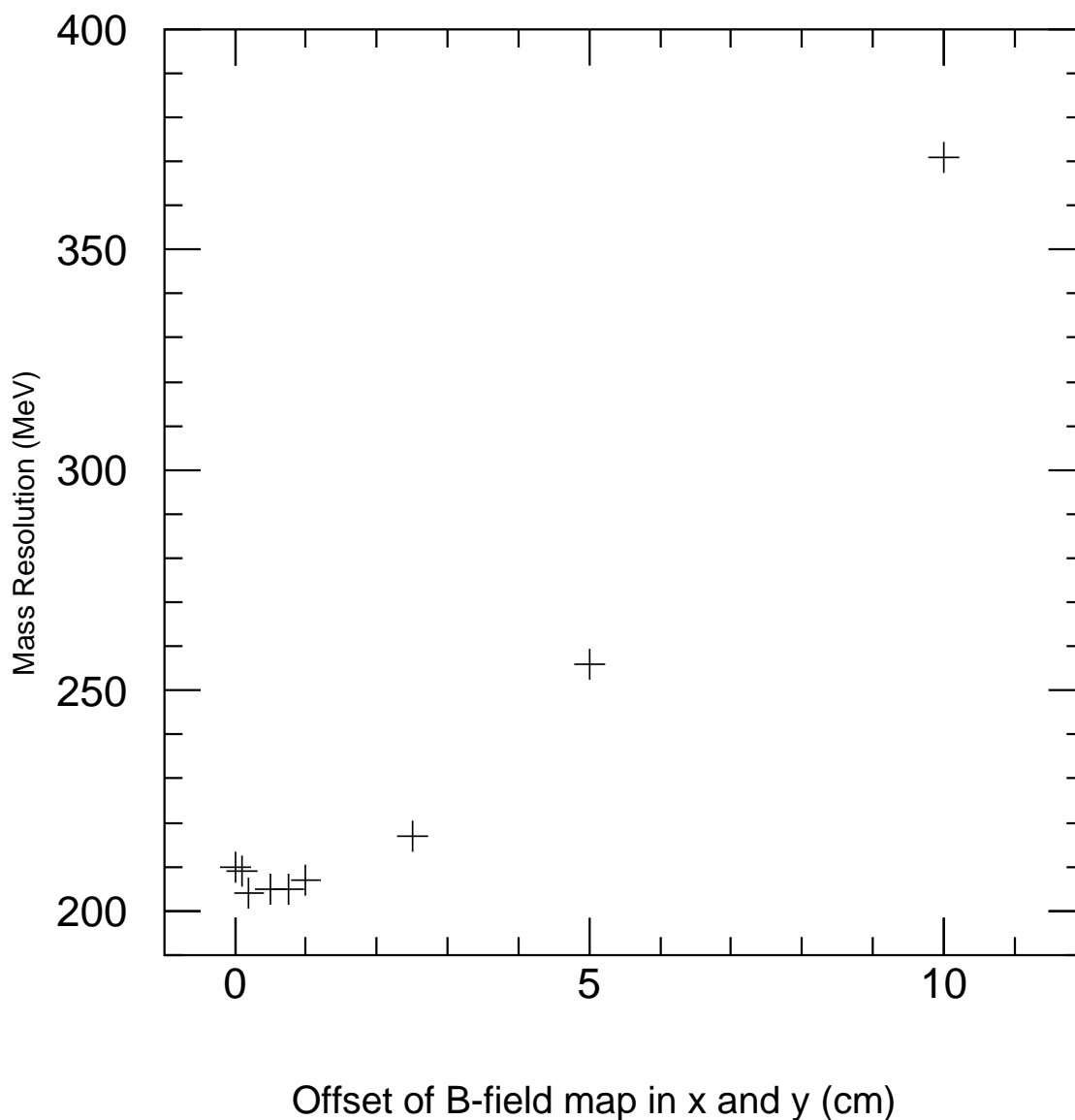


Figure 4.16: The Υ mass resolution in the North arm versus a (x, y) displacement of the magnetic field map. The offset in the figure was applied as $(x, y) \rightarrow (x + \text{offset}, y + \text{offset})$.

the error caused by multiple scattering in the absorber materials so that the opening angle resolution will be determined solely by the absorber material present. For the Υ vector meson mass resolution, the error in the opening angle measurement caused by multiple scattering in the absorber material (which is on the order of 15 mRad) is comparable to the opening angle resolution that would be required if it did not contribute significantly to the mass resolution. (If the error in the mass resolution caused by an opening angle error is to be less than 1%, then the angular resolution that is required for an opening angle of 110° is 14 mRad.) The multiple scattering caused by just the magnet steel is approximately 9 mRad, so the multiple scattering limit if the copper nosecone were not present would be similar.

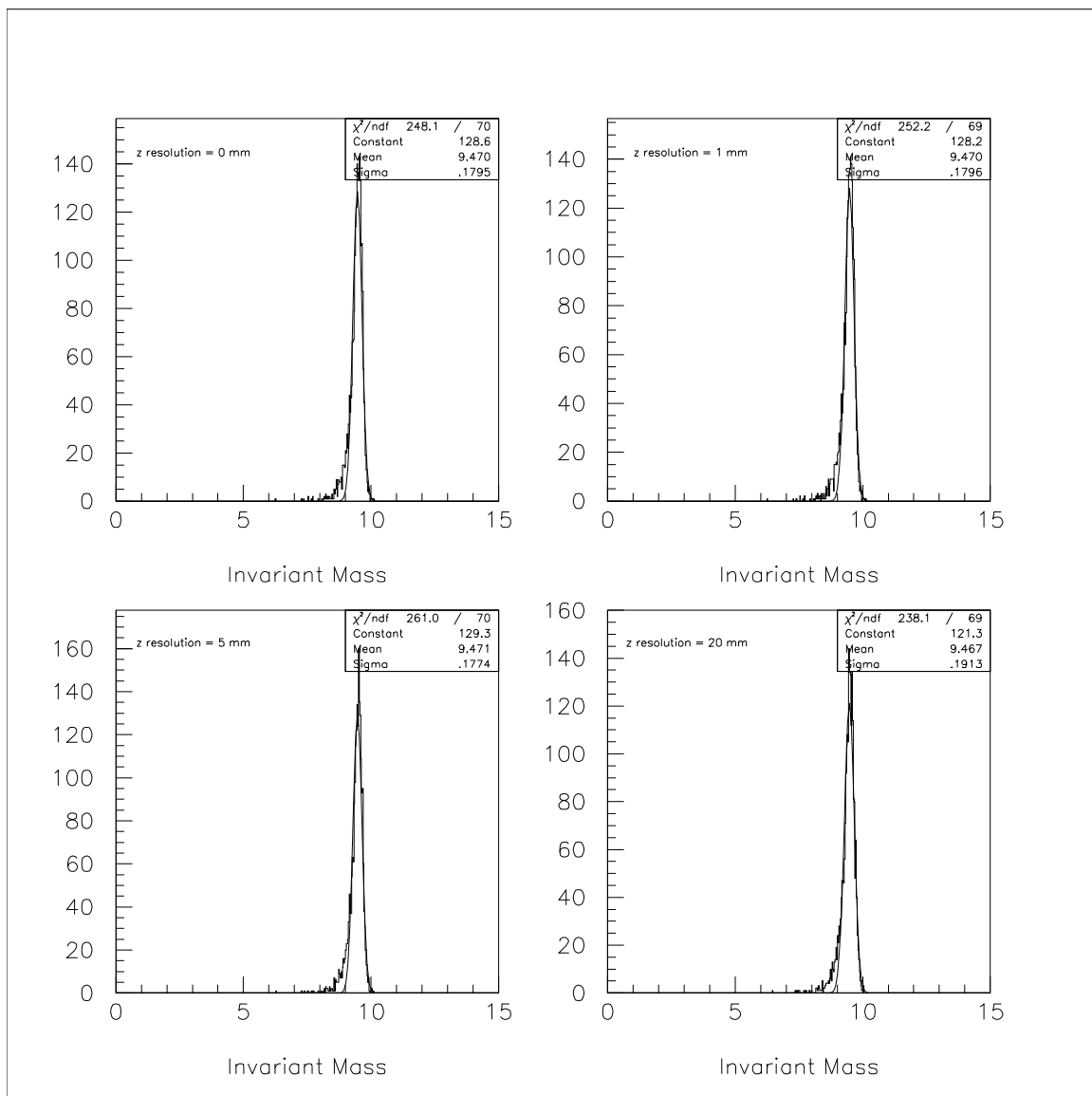


Figure 4.17: The mass resolution in the North muon arm of the Υ versus various vertex z resolutions. (Perfect spectrometer resolutions were used for these calculations so that the contribution from just the projection to the vertex could be seen.)

Because the multiple scattering limit is as small or smaller than the limit that would cause the opening angle error to contribute significantly to the mass resolution, we will determine the alignment requirements by requiring that the opening angle measurement error caused by misalignments be much less than the error caused by multiple scattering.

Since the arms will be independently required to be aligned to the vertex to get good momentum resolutions in the two arms the z alignment of the two arms relative to each other should be taken care of. If in addition the two arms are required to be axially aligned to the beam line, and azimuthally aligned to some common $x - y$ plane target, then the

opening angle measurement should be assured. The θ and ϕ resolutions that are obtained for Υ decay muons with all of the absorber materials present inside the North and South muon arms are approximately 0.4-0.6 mRad inside the tracking volume, and 3-9 mRad at the vertex as shown in Figure 4.18. To retain this angular resolution at the vertex, the displacement of the North arm with respect to the beam axis should be much less than $(1.8 \text{ m})\tan(3 \text{ mRad})=5.4 \text{ mm}$, where 1.8 m is the z distance of station 1 from the interaction point. Similarly, the ϕ alignment with respect to a common (to both arms) alignment point should be much less than 3.0 mRad for the Υ criterion. This corresponds to a displacement at the outer radius of station 1 chambers of $(1.58 \text{ m})\tan(3 \text{ mRad})=4.8 \text{ mm}$. We therefore require that the two muon tracking arms be aligned relative to a common survey point to $5.4/4=1.4 \text{ mm}$ in the τ direction, and to $4.8/4=1.2 \text{ mm}$ in the ϕ direction at the outer radius of station 1 (or to within 0.8 mRad=2.8 arcmin). The z alignment that is required for the individual arms will be more than adequate to provide the arm-to-arm alignment required.

Summary of Alignment Requirements

A summary of the alignment requirements of the muon tracking stations, both internal and global, is given in Table 4.5.

Internal requirements			
	x	y	z
survey	0.025 mm	0.025 mm	0.4 mm
alignment	1.0 mm	1.0 mm	–
Global requirements (survey)			
To Magnet			
	x	y	z
	6.0 mm	6.0 mm	30 mm
To Vertex			
	x	y	z
	1.0 mm	1.0 mm	5.0 mm
North and South Arms			
	x	y	z
	1.2 mm	1.2 mm	5.0 mm

Table 4.5: The internal and global alignment requirements of the muon tracking stations, as determined by simulations.

4.4.2 Alignment Monitors and Survey Requirements

For many of the muon tracker alignments, the structural support of the system will be used to hold the stations in place to within the alignment tolerances (relative to the interaction

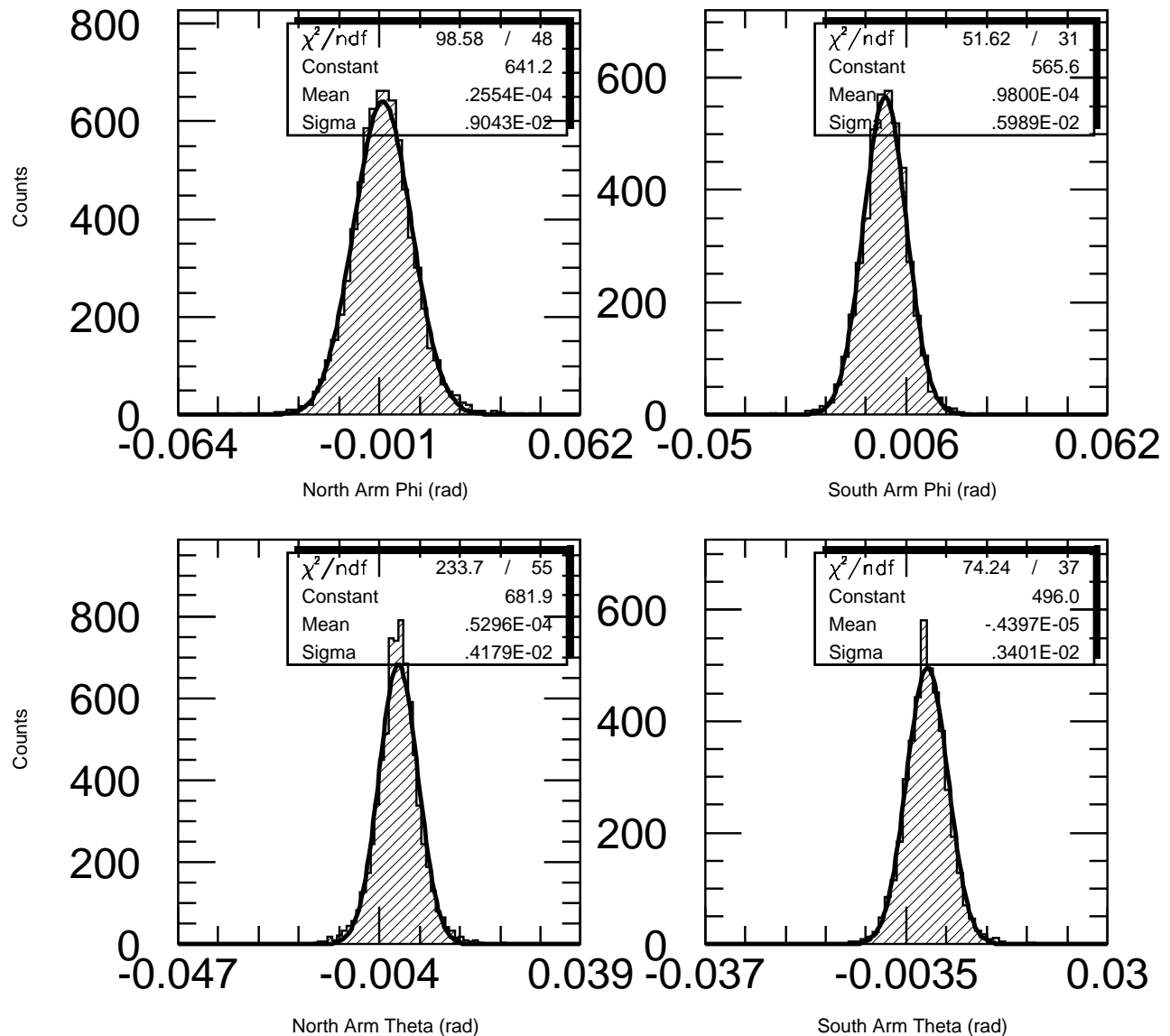


Figure 4.18: The θ and ϕ resolutions obtained by tracking muons from Υ vector mesons through the two muon tracking arms to the vertex. A vertex resolution of 1 mm was used, and the copper nosecone, magnet steel, and copper piston plug absorbers were in place.

point, magnet, etc.) and the exact placements of the tracking stations will be determined by a survey at installation time. For the internal station-to-station survey in the $x - y$ plane, however, we will not only survey the positions at installation time, but also plan to actively monitor the positions with line-of-sight monitors after installation because of the tight survey tolerances.

The station-to-station alignment requirements in z of 0.4 mm should be determined by a survey with respect to the nominal interaction point, as specified by a RHIC or PHENIX survey mark which is used by the whole PHENIX detector. If these surveys can be obtained,

then the survey of the tracking stations to the vertex (or MVD), the muon magnet, and between the two tracking arms should be automatically provided at the same time as long as the survey of the MVD and the magnets are done to a smaller tolerance than the MVD-to-tracking and magnet-to-tracking tolerances.

The placement of the tracking chambers in the $x - y$ plane must be good enough for the active alignment monitors to fall into a line-of-sight so that a final alignment of $25 \mu\text{m}$ can be achieved. Since most active alignment monitor systems that we have looked at are capable of covering a displacement range of 1 to several millimeters, and the global alignment requirements are also on the order of 1 to a few millimeters, we will require the chamber positions to be aligned in the $x - y$ plane relative to a global survey mark to within at least 1 mm. To maintain the alignment of the outside fiducials and/or alignment monitors to the internal cathode strips, tight tolerances will be required during assembly of the chambers. The tolerances that will be maintained have been covered in a muon note [60].

The line-of-sight (LOS) monitoring system which we are most actively pursuing uses several LED-lens-detector systems, with the LEDs mounted at station one, the lenses mounted at station two, and the detectors mounted at station three. Previous work by the GEM muon system [61] has shown that six separate LOS monitors on a chamber are adequate to measure all displacements and rotations which would contribute to an error in the ϕ measurement. If eight monitors are used, then distortions caused by gravitational sag can also be corrected for. We are currently looking at having line-of-site available for as many as three monitors at the outer radius of each chamber plus two monitors at the center of the chamber edges plus two monitors at the bottom edges (small θ) of the chambers. This system would require that the muon tracking volume have several lines-of-sight which extend from station 1 to station 3. For monitors near the piston, this can only be achieved by providing holes in the station 2 chamber frames where lenses could be accurately placed. These lines of sight would also need to be extended through the support structure that is used to hold station 2 in place. Lines of sight at the outer radial edge of station 2 can be provided by making sure that an adequate gap is provided between the outside edge of the chamber frames and the magnet lampshade.

4.4.3 Acceptance for Vector Mesons and Drell-Yan

The muon subsystem's main contribution to the physics of PHENIX comes from observing muon pairs resulting from the decay of vector mesons (ϕ , J/ψ , ψ' , and Υ) and from virtual photon production (the Drell-Yan process). Here we will outline the performance for simple events consisting of correlated pairs of oppositely charged muons. In general, since the addition of the second muon arm, the acceptances have gone up by almost a factor of two from those shown in the PHENIX Conceptual Design Report (CDR) [1]. Since the second arm's piston angle is slightly larger than that of the first arm, 12° compared to 10° , the increase due to the second arm is less than a factor of two, particularly for low-mass events which tend to populate small angles. In addition, for higher-mass events such as the Υ , new acceptance from the muon arms at mid-rapidity is gained from events where one muon goes into each arm.

In all the acceptance calculations used here the dimuon events have been generated based on Vogt's parameterizations[41] except for the Drell-Yan events which are from a structure function calculation. (See Section 4.1.1.) We also assume a muon detection threshold of 2 GeV. Figure 4.19 shows the geometrical acceptance for the vector mesons assuming a flat transverse momentum distribution. It is similar to that shown in the CDR but now has acceptance at negative and central rapidity.

The rapidity and transverse momentum geometrical acceptances for vector mesons are shown in Figure 4.20. The rapidity acceptances for the J/ψ and Υ include bell-shaped peaks at positive and negative rapidities ranging in absolute value from 1.1 to 1.6, and for the Υ a smaller peak at mid-rapidity due to one muon in each of the two arms. For the ϕ , the range in the absolute value of rapidity is 1.8 to 2.4 and because the ϕ events tend to populate small angles the acceptance is much smaller at negative rapidities (second muon arm). All transverse momentum acceptances are roughly flat. The apparent cutoff in the ϕ acceptance near 1.5 GeV/c is due to limited statistics in the simulations.

The acceptance for Drell-Yan events is shown in Figure 4.21 and is similar to that for the Υ . The mass dependence of the acceptance shows a steep decrease for masses lower than about 3 GeV/c², but is close to flat above that.

4.4.4 Signal to Noise for Vector Mesons

The feasibility of the vector meson measurements is dependent on the ratio between the signal muon pairs and the continuum. The continuum pair spectrum arises from a variety of sources including Drell-Yan, charm and beauty pair decays, as well as the combinatoric background due to semileptonic pion decays, kaon decays and misidentified pions. The ratio is also sensitive to the mass resolution of the vector mesons.

A comparison of signal and background sources was given in Figure 3.6 of the PHENIX CDR [1]. It was shown that all of the vector mesons could be recovered by a like sign subtraction. Results of the signal/noise study were used to determine the thickness of the "nosecones" which were added to the central magnet to suppress the semileptonic pion and hadron decay background.

Since the CDR was written, the mass resolutions of the vector mesons have been calculated more accurately and appear to be about 30% larger than expected. This will not cause a significant loss in signal to noise, but will complicate the separation of the Υ 1s and 2s states. It remains possible to improve the signal to noise ratio by applying kinematic cuts to the data which remove the primarily uncorrelated muon background while having only a small effect on the signal. This was shown in Figures 10.31 and 10.32 of the CDR. That gave a signal to noise improvement of a factor of 3 to 6.

The addition of the second muon arm permits the detection of high mass events at low rapidity, complementing the electron arm coverage at lower masses. Since these muons have fairly low momenta, the background is more problematic than for single arm events. Early studies show that the Υ can be recovered with appropriate kinematic cuts, but the dimuon continuum below the Υ will be dominated by combinatorial backgrounds arising from pion and kaon decays.

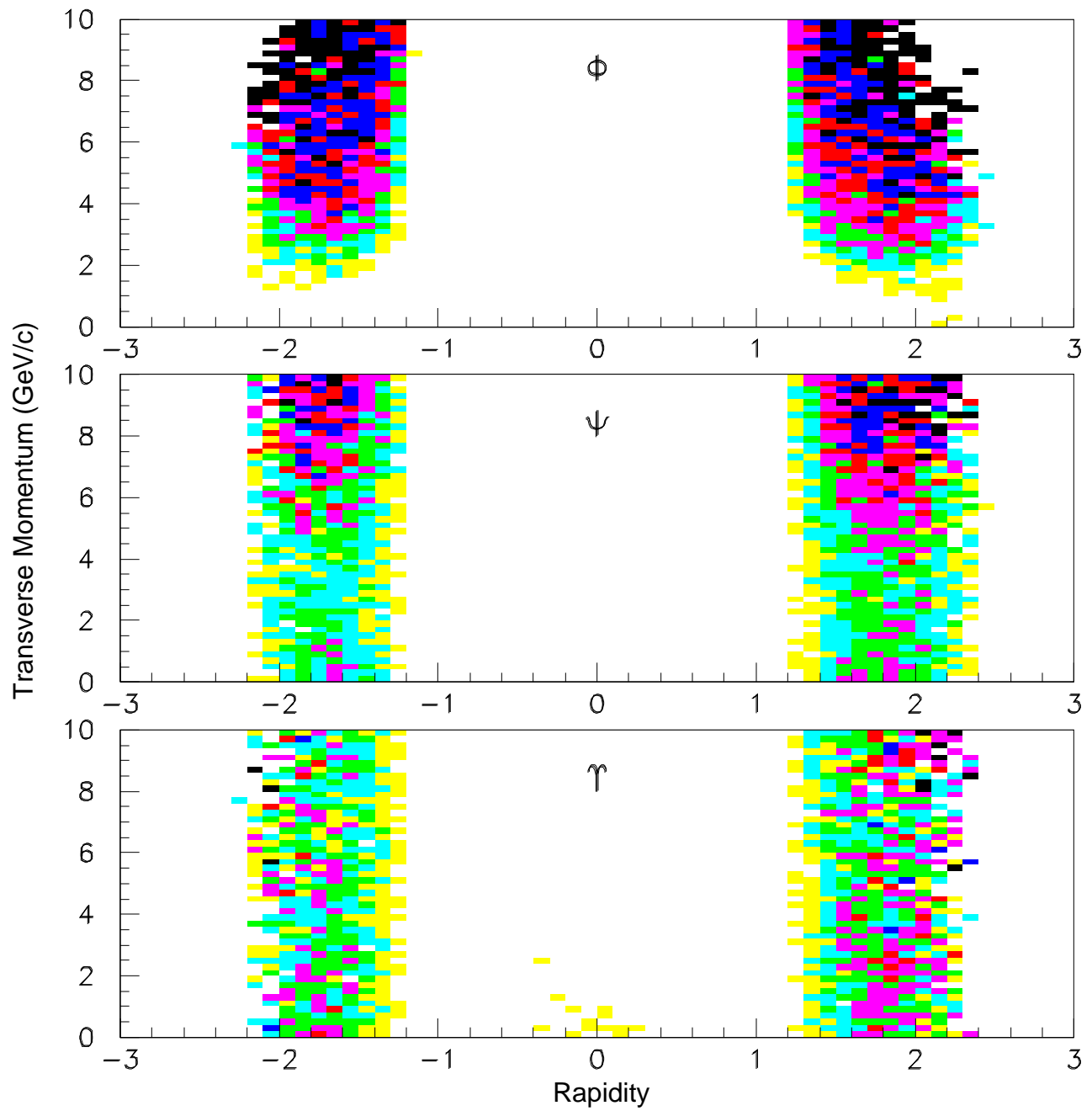


Figure 4.19: Geometrical acceptance in rapidity versus transverse momentum for the ϕ , J/ψ , and Υ .

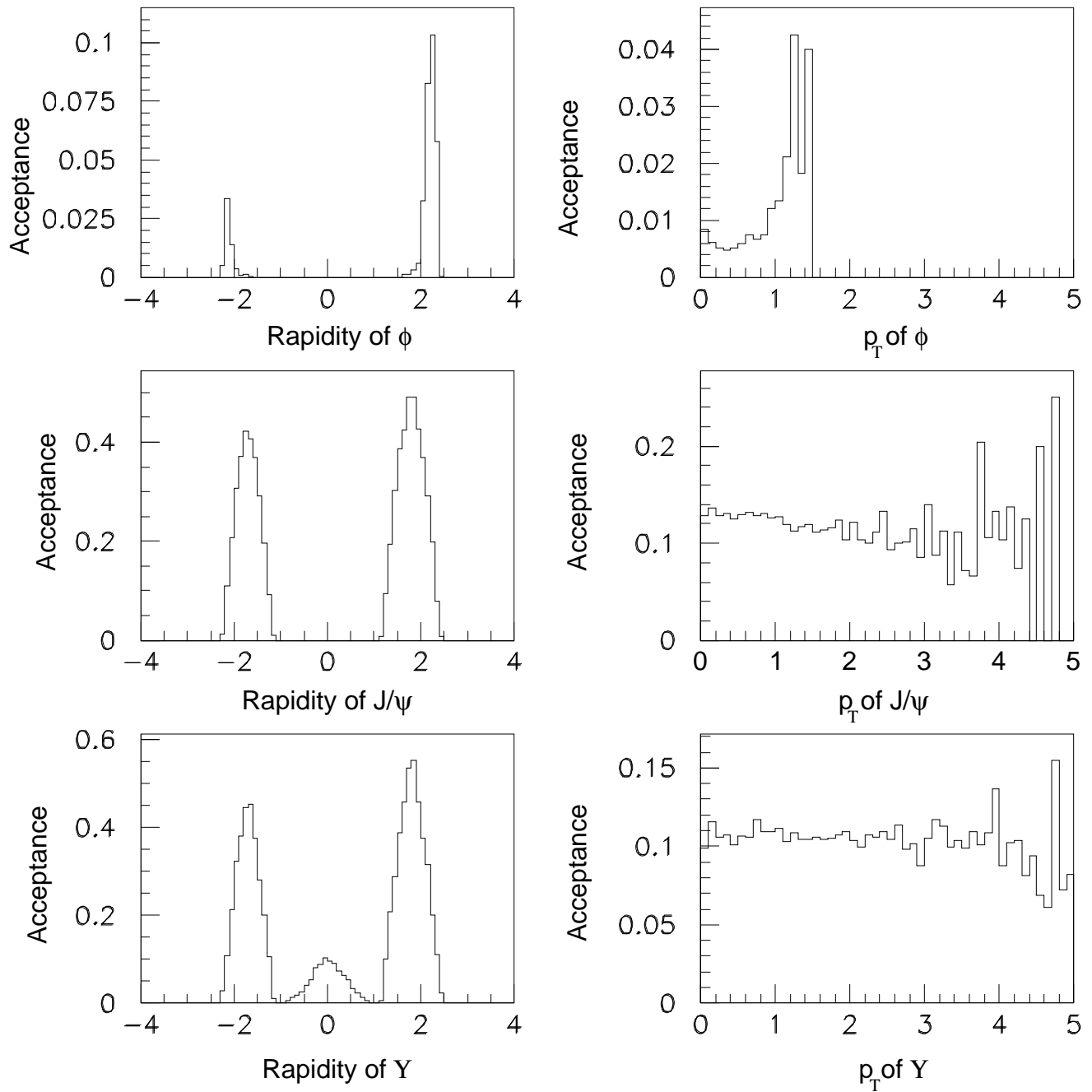


Figure 4.20: Rapidity and transverse momentum dependence of the acceptance for the ϕ , J/ψ , and Υ .

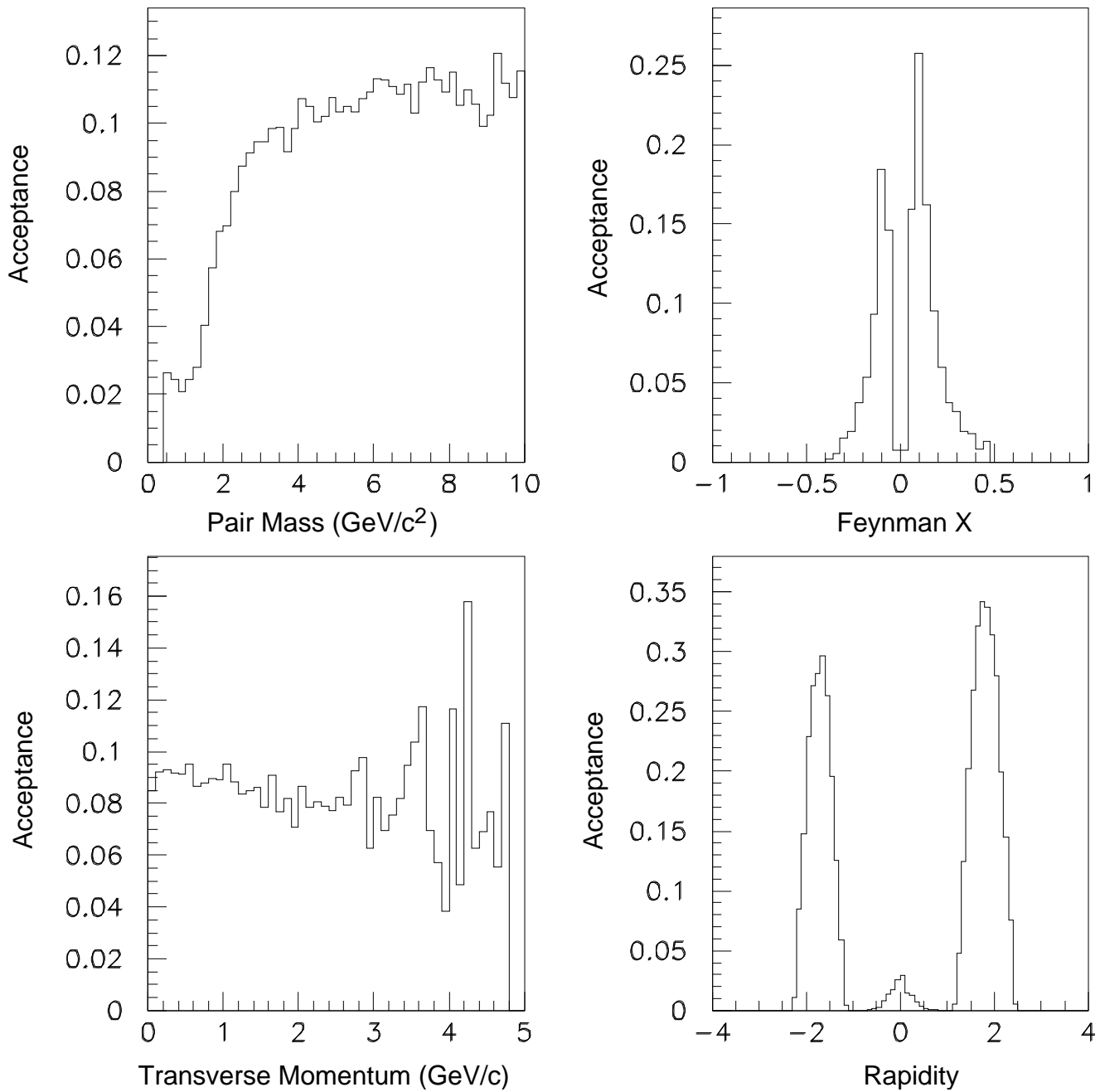


Figure 4.21: The acceptance of dimuons originating from Drell-Yan production as a function of mass x_F , p_T , and rapidity. For the latter three distributions the mass is restricted to 2 to 10 GeV/c^2 .

4.5 Physics Performance Simulations

4.5.1 Rates for Vector Mesons, Drell-Yan and Other Processes

Au-Au Collisions

Table 4.6 shows the expected rates for minimum-bias events from Au-Au collisions, in one RHIC year of running. Contributions from the North muon arm, South muon arm, and from one muon in each of the two arms, are shown separately. The numbers for the North arm are identical to those in the CDR. As in the discussion of acceptances, we see that for higher-mass the South arm adds a little less than a factor of two, because of its larger piston angle; but for the ϕ the increase is only slightly more than 10%. Also, in the ‘‘One in Each’’ column, we see the mid-rapidity yields for higher masses, coming from one muon detected in each of the two arms. For the Υ , the ‘‘One in Each’’ events are nearly as numerous as those observed by detecting both muons in only one arm.

Table 4.6: Counts/RHIC-year for minimum-bias Au-Au collisions, with $p_\mu > 2$ GeV/c

	North Arm	South Arm	One in each
ϕ	500k	69.8k	0
J/ψ	1.73M	1.34M	0
ψ'	24.2k	18.7k	0
Υ	4.92k	4.10k	4.06k
DY(1.5-2.5 GeV)	216k	147k	0
DY(2.5-3.5 GeV)	67k	56k	0
DY(3.5-4.5 GeV)	30k	27k	842
DY(4.5-5.5 GeV)	13k	10k	2.7k
DY(5.5-6.5 GeV)	6.6k	5.5k	3.5k
DY(6.5-7.5 GeV)	3.5k	2.9k	2.5k
DY(7.5-8.5 GeV)	1.8k	1.6k	1.6k

The expected yields as functions of rapidity and of x_2 for one RHIC-year of Au-Au running of the ϕ , J/ψ , Υ and for Drell-Yan (masses in the range 2-10 GeV) are shown in Figure 4.22. A RHIC-year is taken, following the CDR, as 2000 hours at a luminosity of $2.2 \times 10^{27} \text{cm}^{-2} \text{s}^{-1}$.

p-p Collisions

Using scaling from the minimum-bias Au-Au rates above, we can also estimate the $p - p$ yields per RHIC-year at a $p - p$ luminosity of $1.1 \times 10^{31} \text{cm}^2 \text{s}^{-1}$, i.e. the relative rate should be about,

$$\frac{p - p}{\text{Au} - \text{Au}(\text{min} - \text{bias})} = \frac{1.1 \times 10^{31}}{2.2 \times 10^{27}} \times \frac{1}{197^2} = 0.129$$

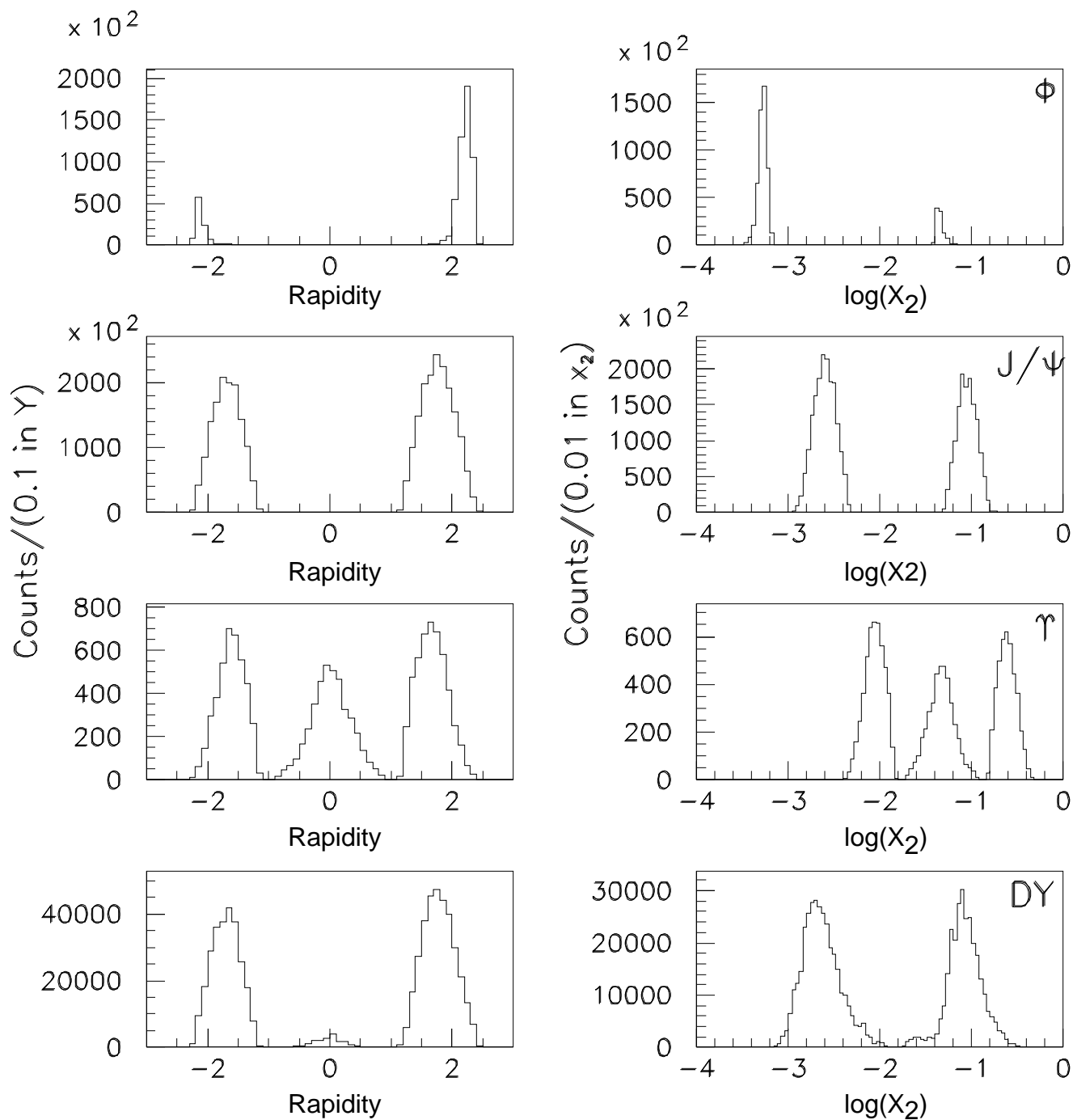


Figure 4.22: Predicted dimuon counts accumulated over one RHIC-year of Au-Au minimum-bias collisions for the ϕ , J/ψ , Υ , and for the Drell-Yan process with mass $> 2 \text{ GeV}/c^2$.

The resulting $p - p$ yields for Drell-Yan are shown in Table 4.7.

Table 4.7: Counts/RHIC-year for p-p collisions with $p_\mu > 2$ GeV

	North Arm	South Arm	One in Each Arm
DY(1.5-2.5 GeV)	28k	19k	0
DY(2.5-3.5 GeV)	8.6k	7.2k	0
DY(3.5-4.5 GeV)	3.9k	3.5k	109
DY(4.5-5.5 GeV)	1.7k	1.3k	348
DY(5.5-6.5 GeV)	850	710	450
DY(6.5-7.5 GeV)	450	370	320
DY(7.5-8.5 GeV)	230	206	206

In addition to the yield performances summarized above, it is also interesting to address the production of, e.g. inclusive muons at $\sqrt{s} = 500$ GeV/c from W boson decays. Some of these processes were studied by Saito and Moss [20]. They showed that the high- p_T (> 25 GeV/c) muon spectra is dominated by W and Z decays, and yields of $\simeq 5 \times 10^3$ events/(1 GeV/c) are expected.

4.5.2 Dimuon Spectra for Au-Au Central Collisions

Signal to Background Ratios for Vector Mesons

Table 10.7 of the CDR presented the estimated signal to noise ratios for all of the vector mesons, which is reproduced here in Table 4.8. The J/ψ and Υ have good signal to noise ratios, while the ψ' is fair and ρ and ϕ are poor. Fortunately the ρ and ϕ yields are quite large, which partly compensates for their low signal to noise.

Table 4.8: Signal to background ratios for the vector meson resonances in the muon detector. Additional kinematical cuts on the accepted tracks can lead to S/N improvements for each of the vector mesons by factors of 3-6.

Resonance	Signal/Background
ρ	1.2×10^{-2}
ϕ	0.8×10^{-2}
J/ψ	2.7×10^0
ψ'	2.1×10^{-1}
Υ	2.9×10^2
Υ'	7.0×10^1

Vector Meson Suppression Sensitivity

One of the primary physics goals of the PHENIX experiment is the measurement of vector meson suppression in central Au-Au collisions, if it occurs. Thus it is important to estimate the sensitivity of the muon arm measurements to small changes in the vector meson yields. This can be done by folding the signal to noise numbers shown above with the expected number of signal events, which were reported in Table 3.3 of the CDR. Assuming that the uncertainties are dominated by the Au-Au central measurements, the errors on the yields of the mesons can be estimated. This is also shown in Table 3.3. For example, in one RHIC year the relative ϕ yield can be measured to 6%, the J/ψ to less than 1% and the Υ to 5%. None of the estimated uncertainties for the vector meson measurements are larger than about 6%. These numbers are for the use of a single muon arm. With both arms it is expected that the uncertainties can be reduced further, based upon the increase in statistics.

4.5.3 Muon-Electron Measurement Capabilities

Charm will be abundantly produced at the RHIC collider. In fact, the leptons from charm decay will probably dominate the low mass dimuon and dielectron continuum. In order to separate the charm decays from the Drell-Yan continuum, it is necessary to obtain an independent measurement of the charm cross section. That should be possible via the measurement of muon-electron coincidences, using the muons arms together with the central electron arms.

Simulation studies of $e - \mu$ measurements were reported in the CDR and shown in Figure 3.8 there. Above about 4 GeV pair mass, charm decays dominate the $e - \mu$ mass spectrum. Below that, semileptonic pion decays and Dalitz decays dominate. The cross-over mass is sensitive to the fraction of Dalitz decays that can be discarded by observing the associated second electron. The yield of $e - \mu$ events is rather large and doubles with the addition of the second muon arm.

4.5.4 Quark Helicity Asymmetry Measurements

The addition of a second muon arm makes possible a program of spin structure function measurements with the PHENIX detector. The two muon arms yield a detector with large acceptance for high mass pairs at central rapidity, as shown in a previous section. These measurements were detailed in the proposal “Spin Structure Function Physics with an Upgraded PHENIX Muon Spectrometer”, written by the PHENIX/Spin Collaboration [62]. Measurement of the asymmetry of Drell-Yan production provides information on the spin structure function of the antiquarks.

In Figure 6 of the upgrade proposal, the predicted asymmetries and uncertainties are shown for a one year run at $\sqrt{s} = 50$ GeV. About 11,000 Drell-Yan dimuons are recorded. Statistical errors on the asymmetries range from 0.02 at $x_2 = 0.04$, to 0.12 at $x_2 = 0.17$, providing a 4 to 5 σ measurement of the antiquark helicity distribution at each of 5 x_2 values.

Production of the W^\pm and Z^0 bosons provide complementary information to Drell-Yan production. W^\pm decays can be detected via the measurement of single high- p_T muons and

Z^0 decays via dimuons. 33,000 W^\pm and 5,000 Z^0 decays can be recorded during a one year run at $\sqrt{s} = 500$ GeV, providing statistical errors on the antiquark helicities similar to those from the Drell-Yan measurements at lower \sqrt{s} .

4.5.5 Gluon Helicity Asymmetry Measurements

Gluon polarization effects can be detected via the asymmetries in heavy quark production. Quarkonium production has the further advantage of relatively easy detection via its large decay width to dimuons. Large numbers of J/ψ , ψ' and Υ pairs can be recorded, over the range $\sqrt{s} = 50$ to $\sqrt{s} = 500$, as shown in Table 2 and Figure 11 of the upgrade proposal. A significant measurement of the gluon polarization is possible over the range of $\sqrt{\tau}$ from 0.006 to 0.2, with the J/ψ and Υ providing independent constraints.

